



HAL
open science

Biocompatible Glyconanoparticles by Grafting of Sophorolipid Monolayers on Monodisperse Iron Oxide Nanoparticles

Andrea Lassenberger, Andrea Scheberl, Krishna Chaithanya Batchu, Viviana Cristiglio, Isabelle Grillo, Daniel Hermida Merino, Erik Reimhult, Niki Baccile

► **To cite this version:**

Andrea Lassenberger, Andrea Scheberl, Krishna Chaithanya Batchu, Viviana Cristiglio, Isabelle Grillo, et al.. Biocompatible Glyconanoparticles by Grafting of Sophorolipid Monolayers on Monodisperse Iron Oxide Nanoparticles. *ACS Applied Bio Materials*, 2019, 2 (7), pp.3095-3107. 10.1021/ac-sabm.9b00427 . hal-02164319

HAL Id: hal-02164319

<https://hal.sorbonne-universite.fr/hal-02164319v1>

Submitted on 25 Jun 2019

HAL is a multi-disciplinary open access archive for the deposit and dissemination of scientific research documents, whether they are published or not. The documents may come from teaching and research institutions in France or abroad, or from public or private research centers.

L'archive ouverte pluridisciplinaire **HAL**, est destinée au dépôt et à la diffusion de documents scientifiques de niveau recherche, publiés ou non, émanant des établissements d'enseignement et de recherche français ou étrangers, des laboratoires publics ou privés.

This document is confidential and is proprietary to the American Chemical Society and its authors. Do not copy or disclose without written permission. If you have received this item in error, notify the sender and delete all copies.

Biocompatible Glyconanoparticles by Grafting of Sophorolipid Monolayers on Monodisperse Iron Oxide Nanoparticles

Journal:	<i>ACS Applied Bio Materials</i>
Manuscript ID	mt-2019-004275.R2
Manuscript Type:	Article
Date Submitted by the Author:	14-Jun-2019
Complete List of Authors:	Lassenberger, Andrea; Institut Laue-Langevin, Scheberl, Andrea; University of Natural Resources and Life Sciences Batchu, Krishna; Institut Laue-Langevin Cristiglio, Viviana; Institut Laue-Langevin, Grillo, Isabelle; Institut Laue-Langevin, Large Scale Structures Group Hermida-Merino, Daniel; Netherlands Organization for Scientific Research, Chemistry Reimhult, Erik; University of Natural Resources and Life Sciences Vienna, Department of Nanobiotechnology Baccile, Niki; CNRS-UPMC, LCMCP UPMC

SCHOLARONE™
Manuscripts

1
2
3
4
5
6
7
8
9
10
11
12
13
14
15
16
17
18
19
20
21
22
23
24
25
26
27
28
29
30
31
32
33
34
35
36
37
38
39
40
41
42
43
44
45
46
47
48
49
50
51
52
53
54
55
56
57
58
59
60

Biocompatible Glyconanoparticles by Grafting of Sophorolipid Monolayers on Monodisperse Iron Oxide Nanoparticles

Andrea Lassenberger,^{a,b} Andrea Scheberl,^a Krishna Chaithanya Batchu,^b Viviana Cristiglio,^b Isabelle Grillo,^b Daniel Hermida Merino,^c Erik Reimhult,^{a,} Niki Baccile^{d,*}*

^aUniversity of Natural Resources and Life Sciences Vienna, Institute for Biologically
inspired materials, Department of Nanobiotechnology, Muthgasse 11/II, 1190 Vienna,
Austria

*erik.reimhult@boku.ac.at

^bInstitut Laue-Langevin, 71 Avenue des Martyrs, 38042 Grenoble Cedex 9, France

^cESRF – The European Synchrotron, 71 Avenue des Martyrs, 38042 Grenoble Cedex 9,
France

1
2
3^dSorbonne Université, Centre National de la Recherche Scientifique, Laboratoire de
4
5
6
7 Chimie de la Matière Condensée de Paris, LCMCP, F-75005 Paris, France
8
9

10
11 *niki.baccile@upmc.fr
12
13
14
15

16 KEYWORDS: sophorolipid, glyconanoparticle, nanoparticle surface functionalization,
17
18
19 small angle neutron scattering, small angle X-ray scattering, lipid shell, iron oxide
20
21
22
23 nanoparticle, core-shell nanoparticle, colloidal stability
24
25
26
27
28
29
30

31 ABSTRACT. This work presents synthesis and characterization of sophorolipid-coated
32
33
34 monodisperse iron oxide nanoparticles. Sophorolipids are biological glycosylated
35
36
37 amphiphiles produced by the yeast *S. bombicola*. In their open acidic form, sophorolipids
38
39
40
41 have been used as surface stabilizing agent for metal and metal oxide nanoparticles but
42
43
44
45 with poor control over size and structural properties. In this work, the COOH function of
46
47
48
49 sophorolipids (SL) was modified with nitrodopamine (NDA), a catechol known for its high
50
51
52
53 affinity to iron ions. The resulting new form of sophorolipid-nitrodopamide (SL-NDA) was
54
55
56
57
58
59
60

1
2
3 used as surface ligand for monodisperse iron oxide nanoparticles. We show, by a
4
5
6
7 combination of thermogravimetric analysis and small angle X-ray and neutron scattering,
8
9
10 that iron oxide nanoparticles (IONP) are stabilized by a single, high-density SL-NDA layer,
11
12
13 which results in excellent colloidal stability under biologically relevant conditions such as
14
15
16
17 high protein and salt concentration. The IONP grafted with SL-NDA showed negligible
18
19
20 uptake and no cytotoxicity tested on two representative cell lines. Thus, they reveal the
21
22
23 potential of sophorolipids as stable and non-toxic surface coatings for IONP-based
24
25
26
27
28 biomedical and biotechnological applications.
29
30
31
32
33
34
35
36
37

38 Introduction

39
40

41 Superparamagnetic iron oxide nanoparticles are used in applications such as drug
42
43
44 delivery, MRI or hyperthermia, for which iron oxide cores smaller than ~20 nm in diameter
45
46
47 are coated with weakly adsorbed polymers (often dextran¹⁻³) or lipids.⁴ However,
48
49
50
51 physisorbed shells lead to low dispersant densities on the particle surface and low
52
53
54
55 colloidal stability over time. Controlled grafting of chemically linked dispersants yields
56
57
58
59
60

1
2
3 denser and more stable shells; therefore, such approaches have received increasing
4
5
6 attention.⁵⁻⁶ With improvements in the synthesis, monodisperse (SD < 5 %) iron oxide
7
8
9 nanoparticles have been developed,⁷ but their hydrophobic (mostly oleic acid) shell of
10
11
12 weakly adhering ligands is not compatible with biomedical applications. Consequently,
13
14
15 the original ligands must be replaced by chemisorbed ligands that provide a water-soluble
16
17
18 and sterically stabilizing shell, crucial for colloidal stability in biological fluids. Ligand
19
20
21 exchange protocols for highly hydrated and chemically grafted ligands, mainly based on
22
23
24 poly(ethylene glycol) (PEG), have therefore been developed.⁸ PEG provides excellent
25
26
27 colloidal stability and long circulation times of the particles in the body due to limited
28
29
30 opsonization (protein binding and elimination of the particles by the reticuloendothelial
31
32
33 system),⁹ but PEG does not provide targeting specificity and has increasingly been
34
35
36 claimed to be subject to antibody production.¹⁰ Coating of nanoparticles with biological or
37
38
39 biomimetic ligands could address both these drawbacks; to this end, other surface ligands
40
41
42 are tested, including carbohydrates.
43
44
45
46
47
48
49
50

51
52 Carbohydrate-grafted nanoparticles are generally referred to as glyconanoparticles¹¹⁻¹²
53
54
55 and they are constituted by a nanoparticle core (e.g. gold or iron oxide) and a shell
56
57
58
59
60

1
2
3 composed of a glycoconjugate, a term which refers to a molecule composed of a
4
5
6
7 carbohydrate on one side and a binding group on the other. Since specific carbohydrates
8
9
10 are known to selectively bind proteins,¹³⁻¹⁵ glyconanoparticles generally contain
11
12
13
14 mannose, galactose, fucose or sialic acid, which are well-known saccharides targeting
15
16
17 carbohydrate receptors on tumor cells.^{14, 16} The binding group must be selected with the
18
19
20 type of core particle surface in mind. Typically, thiols are used to graft to gold
21
22
23
24 nanoparticles while silanes are used to graft to oxide nanoparticles.^{12, 16-17} The main
25
26
27 drawback of these fully synthetic systems is the complex synthesis of the glycoconjugate
28
29
30
31 ligands, mainly due to the classically tedious sugar chemistry, and for this reason
32
33
34
35 alternative routes to prepare glyconanoparticles are worth exploring.
36
37

38
39 In the past fifteen years, a number of research groups has shown the potential of using
40
41
42 natural capping agents for metallic nanoparticles.¹⁸⁻¹⁹ However, the field is still in its
43
44
45
46 infancy due to the poor control over both particle size distribution and composition of the
47
48
49 shell. A promising group of novel capping agents are glycoconjugates obtained through
50
51
52
53 microbial synthesis. This class of molecules, in particular sophorolipids (SL), is the most
54
55
56
57 studied in the field of nanoparticle stabilization. SL are bolaform, non-toxic, bio-based
58
59
60

1
2
3 glycolipids produced by the yeast *Starmerella bombicola* and characterized by a bulky
4
5
6
7 sophorose headgroup and a free carboxyl group.²⁰ SL are known to have natural targeting
8
9
10 abilities, anti-cancer²¹ and anti-bacterial²² properties. SL were previously used to stabilize
11
12
13 metal nanoparticles (Ag, Co)²³⁻²⁵ and iron oxide nanoparticles (IONP).²⁶ The interaction
14
15
16
17 between SL and the nanoparticles was attributed to the complexing of the accessible
18
19
20 COO⁻ group to the surface; however, low grafting densities, poor control over
21
22
23
24 polydispersity, shell composition and even nanoparticle structure show that further
25
26
27
28 enhancement of SL-coated iron oxide nanoparticle synthesis and structure are required
29
30
31 for applications. Here, we propose a new approach based on the use of size-controlled
32
33
34 monodisperse IONP and SL having the COOH group modified with nitrodopamine (NDA)
35
36
37
38 via an amide bond. NDA is an anchor molecule that has been used to bind dispersants
39
40
41 strongly to IONP.²⁷⁻²⁸ We demonstrate grafting of a monolayer SL shell by a combination
42
43
44
45 of SANS and synchrotron SAXS. Furthermore, we show the resulting excellent colloidal
46
47
48
49 stability of the SL-IONP in physiological buffers and protein concentrations, paired with
50
51
52
53 absent cytotoxicity. This work opens opportunities for the application of glycosylated
54
55
56 IONP obtained from natural glycoconjugates, combining strong colloidal stability and
57
58
59
60

1
2
3
4 water solubility with the imaging, tracking and therapeutic abilities contributed by the
5
6
7 IONP core.
8
9

10 11 12 13 **Experimental Section**

14
15
16 **Materials.** All Chemicals were purchased from Sigma-Aldrich and all solvents from
17
18
19 Roth. Chemicals were used as received without further purification (see supporting
20
21
22 information for details). Sophorolipids (Sopholiance, batch number: 11103A, dry content:
23
24
25
26 60 ± 6 %) are purchased from Soliance, France.
27
28
29

30
31 **Synthesis of sophorolipids (SL).** Acidic sophorolipids have been prepared from a
32
33
34 commercial batch of a sophorolipid mixture using alkaline hydrolysis to convert the crude
35
36
37 lactonic/acidic mixture into a fully acidic sophorolipid compound. Extraction and
38
39
40 purification have been performed using the method N°2 described earlier,²⁹ to which one
41
42
43 should refer for a typical ¹H solution NMR fingerprint. The compound used here is majorly
44
45
46
47 (> 80%) composed of the acidic subterminal C18:1-*cis* form that forms micelles.³⁰
48
49
50

51
52 **Synthesis of nitrodopamide-SL (SL-NDA) ligands.** 6-Nitrodopamine-hemisulfate (NDA-
53
54
55 HSO₄) was synthesized according to literature with slight modifications.³¹ SL-NDA was
56
57
58
59
60

1
2
3 synthesized by (1-cyano-2-ethoxy-2-oxoethylideneaminoxy)dimethylamino-morpholino-
4
5
6
7 carbenium hexafluorophosphate (COMU) mediated peptide-coupling reactions.³²⁻³³
8

9
10 Briefly, 100 mg (0.16 mmol) of SL were pre-activated with 1.5 eq COMU and 1 eq *N*-
11
12 methylmorpholine in 7 mL dimethylformamide (DMF) at RT for 10 minutes. The mixture
13
14 was cooled to 0 °C and a mix of 1eq NDA and 1eq *N*-methylmorpholine in 5 mL DMF was
15
16
17 slowly dropped to the activated acid. The mixture reacted for 1 h at 0 °C and subsequently
18
19
20
21
22
23
24 3 h at RT. The solvent was evaporated and 4 mL of Milli-Q were added to the crude
25
26
27
28 product. The product was transferred into butanol (BuOH) and extracted thrice with Milli-
29
30
31 Q, once with 1.5 M HCl and finally washed with pure Milli-Q. BuOH was evaporated and
32
33
34 the product was vacuum-dried. The coupling of SL to NDA was confirmed by FTIR and
35
36
37
38 by solution ¹H NMR (see Figure S1 for details), showing the coexisting 1:1 ratio between
39
40
41
42 SL and NDA together with the downfield shift, from 3.05 ppm to 3.47 ppm, attributed to
43
44
45 the α -CH₂ in NDA and respectively in an amine and amide environment.^{32, 34} One can
46
47
48 also observe the parallel upfield shift, from 2.30 ppm to 2.18 ppm of α -CH₂ in SL for
49
50
51
52 respectively an amine and an amide environment. NMR excludes the presence of
53
54
55 unreacted free NDA, but we must acknowledge the presence of residual COMU and
56
57
58
59
60

1
2
3 unreacted SL (between 10 and 20 mol% with respect to SL-NDA), which due to similar
4
5
6
7 physico-chemical properties were not removed by washing the sample. However, COMU
8
9
10 and unreacted SL do not have the affinity to the iron oxide nanoparticle surface to displace
11
12
13
14 oleic acid or interfere with the ligand displacement by SL-NDA.
15
16

17 **Synthesis of iron oxide nanoparticles (IONP).** Iron oxide NP (3-10 nm in diameter)
18
19
20 coated with oleic acid (OA) were synthesized by thermal decomposition of iron
21
22
23 pentacarbonyl according to a heat-up procedure originally proposed by Hyeon *et al.*³⁵ that
24
25
26
27 was slightly modified as described in ⁸. Details for the molar ratios of reactants can be
28
29
30
31 found in the supporting information (Table S1). Larger, 14.1 nm IONP were synthesized
32
33
34
35 via a modified two-step method introduced first by Park *et al.*³⁶ and previously by us.⁹
36
37
38 IONP cores with diameters of 3.1, 4.6 and 14.1 nm were used for functionalization with
39
40
41
42 sophorolipids and further experiments.
43
44

45 **Ligand exchange and purification.** SL-IONP were synthesized according to a slightly
46
47
48 modified method published earlier.⁸ For 4.6 nm cores, 0.9 g of as-synthesized IONP
49
50
51 coated with oleic acid were dispersed in 20 mL DMF. 0.183 g of SL-NDA were added and
52
53
54
55
56 the mixture was sonicated for 28 h at slightly elevated temperature. Amounts of ligand
57
58
59
60

1
2
3 were adjusted for the smaller 3.1 nm IONP to account for the difference in surface area
4
5
6 and the same surface area to ligand ratio was used. However, for the 14.1 nm cores we
7
8
9
10 used a much larger excess of ligand (10x with respect to surface area), supposing that a
11
12
13 larger excess of ligand will aid in achieving a high surface coverage. After ligand
14
15
16 exchange, the SL-IONP were washed three times with n-hexane to remove released OA.
17
18
19
20
21 In a final step, the solvent was evaporated and the IONP were lyophilized. The lyophilized
22
23
24 SL-IONP were redispersed in Milli-Q and dialysed in a 12-14 kDa MWCO dialysis bag
25
26
27 against 5 L Milli-Q to remove excess SL-NDA ligands. Alternatively, SL-IONP were
28
29
30 purified by repeated (5x) membrane centrifugation in 50 kDa MWCO Amicon filter units.
31
32
33
34
35 The purified SL-IONP were lyophilized and could be stored for more than two years as a
36
37
38 dark-brown powder. The yield was 96 % calculated with respect to the initial amount of
39
40
41 IONP cores. SL-IONP were analyzed by TEM, TGA, ATR-FTIR and DLS.
42
43
44

45 The samples were named according to their core diameter measured by TEM: 3.1 nm
46
47
48 SL-IONP (diameter 3.1 nm), 4.6 nm SL-IONP (diameter 4.6 nm) and 14.1 nm SL-IONP
49
50
51 (diameter 14.1 nm)
52
53

54
55
56 **Cell growth.** U937 cells were grown under conditions reported in ⁹.
57
58
59

1
2
3
4 **Toxicity test.** Toxicity measurements were performed with the PrestoBlue® Cell Viability
5
6
7 assay. Briefly, 2×10^4 cells were seeded on 96-well plates using 200 μl medium per well
8
9
10 and incubated for 16 h (each 6 repeats for sample and control). 5 μl nanoparticle
11
12
13 dispersion (1 mg Fe/ml) were added and incubated for either 2 or 20 h. As control 5 μl
14
15
16 Milli-Q water were added. After incubation, 20 μl PrestoBlue® were added and plates were
17
18
19 incubated for one hour. A Tecan infinite F200 plate reader with excitation filter 560 ± 20
20
21
22 nm and emission filter 595 ± 35 nm was used to read the plates. The background was
23
24
25
26
27 determined by measuring medium with presto blue at 10 % (v/v).
28
29
30

31 Viability was calculated as:

$$\frac{X}{X_c} * 100 \% \quad (1)$$

32
33
34
35
36
37
38
39
40 with X the average value determined for cells incubated with SL-IONP and X_c the
41
42
43 average value measured for control cells.
44
45
46

47 **SL-IONP uptake by cells and iron quantification.** For uptake experiments, 2×10^6 cells
48
49
50 (monocytes) and 1×10^6 cells (MCF-7) were seeded in a total volume of 5 ml in 6-well
51
52
53 plates and incubated for 12 h. 50 μL of a 1 mg/mL Fe dispersion of SL-IONP were added
54
55
56
57
58
59
60

1
2
3 and the cells were incubated for 20 hours. The control well was incubated with 50 μ L Milli-
4
5
6
7 Q water. After incubation, cells were centrifuged and consequently washed three times
8
9
10 with PBS to remove IONP that were not taken up the cells. Iron quantification was done
11
12
13 by a modified Ferrozine test as described previously.⁹ For each type of SL-IONP at least
14
15
16
17 5 wells were prepared in parallel and 3 independent repetitions were performed, resulting
18
19
20
21 in a minimum of 9 data points for each type of SL-IONP.
22
23

24 **Protein quantification.** The Rotitm-NanoQuant protein detection assay was used for
25
26
27 protein quantification according to the manufacturer's protocol. BSA dissolved in 50 mM
28
29
30 NaOH was used as a standard.
31
32
33

34
35 **Transmission electron microscopy (TEM) and analysis.** TEM images were recorded on
36
37
38 a FEI Tecnai G2 20 transmission electron microscope at 160 kV for low resolution and
39
40
41 200 kV for high resolution imaging. Samples were drop-casted from toluene dispersions
42
43
44 (IONP capped by oleic acid) or aqueous dispersions (SL-IONP) onto a 300-mesh carbon-
45
46
47 coated copper. The Pebbles³⁷ software package was used to determine the size
48
49
50
51
52 distributions from the micrographs. Approximately 900 IONP were used for size
53
54
55
56 determination by Pebbles for each sample of nanoparticles.
57
58
59
60

1
2
3
4 **Transmission Electron Microscopy experiments under cryogenic conditions (cryo-**
5
6
7 **TEM).** Cryo-TEM images were recorded on a FEI Tecnai 120 twin microscope at 120 kV
8
9
10 with a Gatan Orius CCD numeric camera and a Gatan Cryoholder (Gatan 626DH, Gatan).
11
12
13 DigitalMicrograph™ software was used for image acquisition. A custom-built device was
14
15
16 used for cryo-fixation. SL-IONP aqueous dispersions and SL-NDA solutions were
17
18
19 deposited on glow-discharged holey carbon copper grids (Quantifoil R2/2, Germany). The
20
21
22 grids were immediately plunge-freezed by dipping into liquid ethane at -180 °C and
23
24
25 transferred into liquid nitrogen. All grids were stored in liquid nitrogen.
26
27
28
29
30

31 **Thermogravimetric Analysis (TGA).** TGA data were measured using a Mettler-Toledo
32
33
34 TGA/DSC 1 STAR System in a temperature range of 25-650 °C with 10 K/min. A stream
35
36
37 of 80 mL/s of synthetic air was used to ensure complete combustion of the SL-NDA
38
39
40 ligands since NDA is known to polymerize by pyrolysis under N₂. 0.5 - 1.5 mg sample
41
42
43 were measured, The total organic content (TOC) was calculated as the fraction of mass
44
45
46 loss up to 650 °C.
47
48
49
50
51

52 **Dynamic Light Scattering (DLS).** DLS was measured on a Malvern Zetasizer Nano-ZS
53
54
55 at 20 °C. Instrument settings: Fe₃O₄, Milli-Q as dispersant (0.89 mPa·s, RI=1.33), 3
56
57
58
59
60

1
2
3 individual measurements were performed with 13 runs of 10 s each. All samples of SL-
4
5
6
7 IONP were measured at a concentration of 0.5 mg_{Fe}/mL. The nanoparticles were
8
9
10 dispersed in water (2 mg/mL) and 10 % fetal calf serum for experiments in which the
11
12
13 temperature was varied from 20 °C to 70 °C and back with 5 °C steps and an equilibration
14
15
16 time of 2 minutes. At each temperature, 3 individual measurements with 13 runs of 10 s
17
18
19
20
21 were recorded.
22
23

24 **¹H Nuclear magnetic resonance (NMR) measurements.** ¹H NMR data were acquired on
25
26
27 a Bruker Avance III 300 spectrometer using a 5 mm ¹H-X BBFO probe, 16 transients with
28
29
30 1 s recycling delay. The value chemical shifts (δ) are reported in ppm at 298 K using
31
32
33 tetramethylsilane (TMS) as reference. MeOD-d₄ was used as solvent. COSY spectra
34
35
36 were acquired using a standard pulse program from the Avance III library, with 1 s
37
38
39 recycling delay, 8 transients per scan and 256 spectra acquired in the F1 dimension.
40
41
42
43
44
45
46
47
48

49 **Attenuated total reflection – Fourier transform infra-red (ATR-FTIR) measurements.** IR
50
51
52 spectra of the lyophilized samples were recorded on a Perkin Elmer 400 FTIR
53
54
55
56
57
58
59
60

1
2
3 spectrometer with diamond single-reflection ATR equipment and a resolution of 4 cm^{-1} ,
4
5
6
7 averaging 32 scans.
8
9

10 **Small Angle X-ray Scattering (SAXS).** SAXS patterns were measured using a Dectris-
11
12 Pilatus 1M detector with a resolution of 981×1043 pixels and a pixel size of 172×172
13
14 μm at the Dutch-Belgian Beamline (DUBBLE) station BM26B of the European
15
16
17 Synchrotron Radiation Facility (ESRF) in Grenoble, France. The sample to SAXS detector
18
19
20
21 distance was set to ca. 3100 mm using a wavelength of 1.033 \AA . SAXS patterns were
22
23
24
25
26
27
28 integrated azimuthally to obtain a typical $I(q)$ spectrum. A quartz capillary, used as
29
30
31 sample holder, was filled with Milli-Q grade water, used as solvent, and then with the
32
33
34
35 sample dispersion. To eliminate errors in the background subtraction process due to in
36
37
38 homogeneities of the capillary walls, great care was taken to analyze both the water and
39
40
41
42 sample solutions at the same position. Solvent contribution was subtracted during the
43
44
45 data treatment. Data were corrected for the transmission of the direct beam and
46
47
48
49 presented in absolute scale. The q-range calibration was made using a silver behenate
50
51
52 standard sample ($d_{ref} = 58.38 \text{ \AA}$)
53
54
55
56
57
58
59
60

1
2
3 **Small Angle Neutron Scattering (SANS).** SANS was performed at the Institut Laue-
4 Langevin (ILL, Grenoble, France) on D16 and D33 beamlines. The spectrometer
5
6 configurations were adjusted as follows. *D16 beamline* ($3.5 \cdot 10^{-2} \text{ \AA}^{-1} < q < 0.5 \text{ \AA}^{-1}$): neutron
7 wavelength, $\lambda = 4.5 \text{ \AA}$, sample-to-detector distance = 955 mm, sample and detector
8
9 rotation angles: $\omega = 5.5^\circ$ and $2\theta = 11^\circ$, acquisition time = 60 min. *D33 beamline* ($5.0 \cdot 10^{-3}$
10
11 $\text{ \AA}^{-1} < q < 0.3 \text{ \AA}^{-1}$): neutron wavelengths: $\lambda_1 = 4.6 \text{ \AA}$ and $\lambda_2 = 13.0 \text{ \AA}$ sample-to-detector
12
13 distances = 2 m, 10 m, acquisition time = 10 min (in D₂O), 45 min (in MeOD-d4). For both
14
15 spectrometers: neutron absorber: Boron Carbide (B₄C), thickness of quartz Hellma cells:
16
17 1 mm, temperature (controlled): $T = 25^\circ\text{C}$, background: 99.9 % D₂O. Direct beam, empty
18
19 cell and H₂O were also recorded for both spectrometers. The background sample (D₂O)
20
21 signal was subtracted from the experimental data. q is defined as $(4\pi/\lambda)\sin\vartheta/2$ where ϑ
22
23 is the scattering angle between the incident and the scattered neutron beams. Data
24
25 treatment was done with the home-made software package provided at the beamline.
26
27 Direct determination of the number of neutrons in the incident beam and the detector cell
28
29 solid angle allowed obtaining absolute values of the scattering intensity. The acquired 2-
30
31 D raw data were corrected for the scattering of the ambient background and the empty
32
33
34
35
36
37
38
39
40
41
42
43
44
45
46
47
48
49
50
51
52
53
54
55
56
57
58
59
60

1
2
3
4 cell. Further, the data were normalized by the neutron flux on the samples to yield an
5
6
7 absolute scale (cross section per unit volume). The data were radially averaged to yield
8
9
10 the 1-D intensity distribution $I(q)$.
11
12

13
14 **Fit of small angle scattering data (SAXS, SANS).** All data presented were fitted using a
15
16
17 classical core-shell sphere form factor model (assuming a unitary structure factor in the
18
19
20 analyzed range of q -values),³⁸ using the SasView 3.1.2 software (CoreShellModel)
21
22
23 available free of charge on the developers' website.³⁹ In the model, we consider the core
24
25
26 to be composed of iron oxide and the shell of a homogeneous SL-NDA layer of variable
27
28
29 thickness. One should be aware that this is a strong approximation, because SL-NDA
30
31
32 could be described by at least three different regions of inequivalent densities: sophorose,
33
34
35 oleic acid and NDA. Nonetheless, the goal of the fitting analysis in this work is not to
36
37
38 precisely describe the morphology of the of the nanoparticle shell, but to demonstrate that
39
40
41
42 SL-IONP have a shell with a thickness compatible with a monolayer of SL-NDA; the
43
44
45 homogeneous core-shell model provides an adequate model with a minimum number of
46
47
48 fitting variables to determine the presence and thickness of a reasonably homogeneous
49
50
51
52 shell. All theoretical and technical details of both the model and fitting function can be
53
54
55
56
57
58
59
60

found at on the developers' homepage.³⁹ The following parameters (Table 1) characterize the fitting function:

Table 1. Structural parameters used in the core-shell sphere model to fit both the SANS and SAXS data recorded for the SL-IONP.

Parameter	Description	Fixed	Variable
d	Core diameter	x	
t	Shell Thickness		x
ρ_c	Scattering Length Density (SLD) of the IONP core	x	
ρ_s	Scattering Length Density (SLD) of the SL shell		x
ρ_{solv}	Scattering Length Density (SLD) of the solvent (H ₂ O and D ₂ O for X-ray and neutron scattering experiments respectively)	x	
scale	Volume fraction	x	
background	Background level		x
PDI	Polydispersity		x

The fixed parameters of the fitting function vary according to the type of technique used to study the samples. The fixed values which we have used in this work are reported

hereafter. The nanoparticle diameter d is determined independently by TEM and SAXS.

The SLD values have been determined using the SLD calculator tool in the SasView

software. $\rho_{solv}(\text{X-ray}) = 9.410 \times 10^{-6} \text{ \AA}^{-2}$ and $\rho_{solv}(\text{neutron}) = 6.4 \times 10^{-6} \text{ \AA}^{-2}$, where $\rho_{solv}(\text{X-}$

ray) and $\rho_{solv}(\text{neutron})$ respectively refer to the X-ray and neutron SLD of H_2O and D_2O . ρ_c

(X-ray) = $40.0 \times 10^{-6} \text{ \AA}^{-2}$ and $\rho_c(\text{neutron}) = 6.9 \times 10^{-6} \text{ \AA}^{-2}$ refer to the X-ray and neutron

SLD of iron oxide respectively, for which we have used the bulk density value of 5.17

$\text{g}\cdot\text{cm}^{-3}$. Polydispersity was allowed to vary between 0.1 and 0.15 and the volume fraction

was set to 0.4 % for samples 3.1 nm SL-IONP and 4.6 nm SL-IONP and to 0.1 % for

sample 14.1 nm SL-IONP, the smaller value coming from the larger amount of SL-NDA

in the 14.1 nm SL-IONP sample (please refer to main text for more details). In the final

fitting procedure, t and ρ_s are the only structural variable parameters, while the

background level is set as variable mainly to adjust the quality of the final fit. The typical

size and composition of SL-NDA also imposes several constraints on the effective t and

ρ_s values. One can reasonably consider $2.0 < t \text{ (nm)} < 3.5$ for a single SL-NDA layer,

where the lower and upper limits consider plausible molecular bending and stretching;

meanwhile, $9.6 < \rho_s \text{ (X-ray)} (10^{-6} \text{ \AA}^{-2}) < 12$ and $1 < \rho_s \text{ (neutron)} (10^{-6} \text{ \AA}^{-2}) < 5$ reasonable

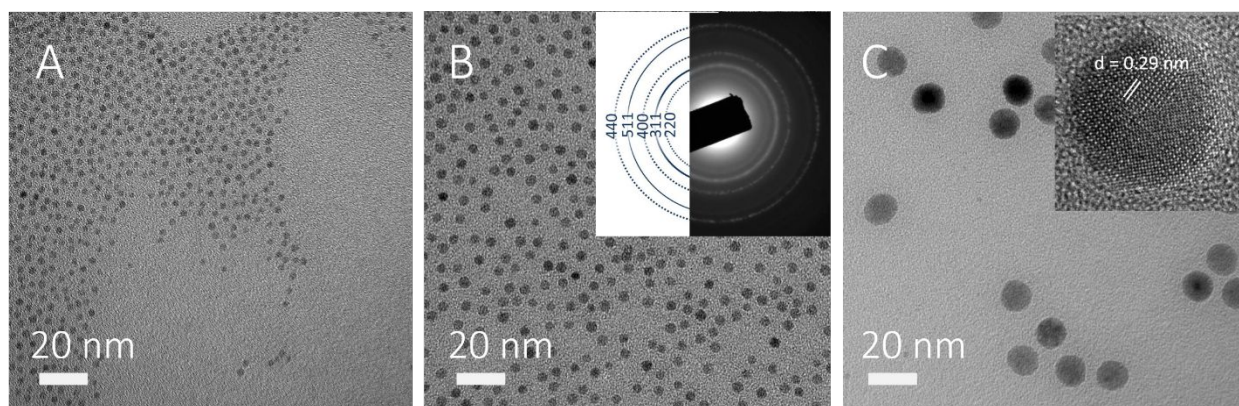
1
2
3
4 identify the range for both the X-ray and neutron shell SLD values, which can vary
5
6
7 between a highly hydrated shell and a poorly hydrated organic layer.
8
9

14 Results and Discussion

15
16
17 **IONP synthesis, ligand exchange and purification.** Spherical, monodisperse and single-
18
19
20 crystalline iron oxide nanoparticles with diameters of 3.1 ± 0.3 nm ($\sigma = 8.0$ %), 4.6 ± 0.3
21
22
23 nm ($\sigma = 7.0$ %) and 14.1 ± 0.9 nm ($\sigma = 6.9$ %) were synthesized and characterized by
24
25
26
27 HR- and LR-TEM. Figure S2 shows TEM micrographs of as-synthesized monodisperse
28
29
30
31 oleic acid-coated iron oxide cores.
32
33

34
35 The exchange of hydrophobic oleic acid for sophorolipid-nitrodopamide ligand was
36
37
38 performed using a method established earlier⁸ and yielded well-dispersed SL-NDA
39
40
41 coated IONP (SL-IONP) with three different core sizes (Figure 1). Single-crystallinity of
42
43
44 the IONP cores was revealed by HR-TEM (inset in Figure 1C and Figure S3) and the
45
46
47 lattice spacing in the (220) direction was measured to be 0.29 nm. The electron diffraction
48
49
50 pattern (inset Figure 1B) shows the high crystallinity of the IONP. The determined ratios
51
52
53 of d -spacings show good agreement with the JCPDS database values given for
54
55
56
57
58
59
60

1
2
3 maghemite or magnetite.⁴⁰ Single-crystalline iron oxide nanoparticles (magnetite and
4
5
6
7 maghemite) in this size-range are known to be superparamagnetic, thereby possessing
8
9
10 attractive properties for biomedical imaging and drug delivery.
11
12
13
14
15



31 **Figure 1.** TEM micrographs of three sizes of SL-IONP of sizes A) 3.1 ± 0.3 nm, B) $4.6 \pm$
32 0.3 nm and C) 14.1 ± 0.9 nm. The insets in B) and C) show the electron ring diffraction
33
34
35
36
37
38
39
40
41
42
43
44
45
46
47
48
49
50
51
52
53
54
55
56
57
58
59
60
pattern and a high-resolution micrograph of 14.1 nm IONP, revealing the high crystallinity
of the single crystal cores.

To demonstrate colloidal stability of SL-grafted IONP, excess ligand should be removed
from the nanoparticle dispersion. Thus, SL-IONP were purified using two common

1
2
3 purification methods for nanoparticles, namely dialysis and membrane centrifugation to
4
5
6
7 remove the excess of the micelle-forming glycolipid ligand.
8
9

10 The functionalization of the IONP with SL-NDA through ligand replacement was first
11
12 evaluated using ATR-FTIR. Figure 2 shows the FTIR spectra of the compounds and
13
14 products. NDA has a characteristic C-O stretch band at 1272 cm^{-1} ,⁴¹ which can be found
15
16
17 in the product of the purified SL-NDA but not in pure SL. Likewise, the “sugar bands”
18
19
20 corresponding to C-O and C-O-C stretch modes at 1021 cm^{-1} and 1069 cm^{-1} ,⁴²
21
22
23 respectively, from the sophorolipid are also strong in the SL-NDA product. Finally, the
24
25
26 bands of the amide bond formed between SL and NDA are clearly visible in SL-NDA.
27
28
29
30
31
32
33
34
35 Figure 2 shows that two characteristic bands of oleic acid, the C=O stretch at 1707 cm^{-1}
36
37
38 (which is slightly higher than for sophorolipid) and the out-of-plane O-H stretch at 963
39
40
41
42 cm^{-1} are absent or insignificant compared to the characteristic bands of the sophorolipid
43
44
45 and NDA.³² In summary, the ATR-FTIR results strongly support successful ligand
46
47
48
49 replacement of the oleic acid by SL-NDA to form iron oxide nanoparticles with a shell of
50
51
52
53
54
55
56
57
58
59
60
sophorolipid, strongly linked by nitrodopamide.

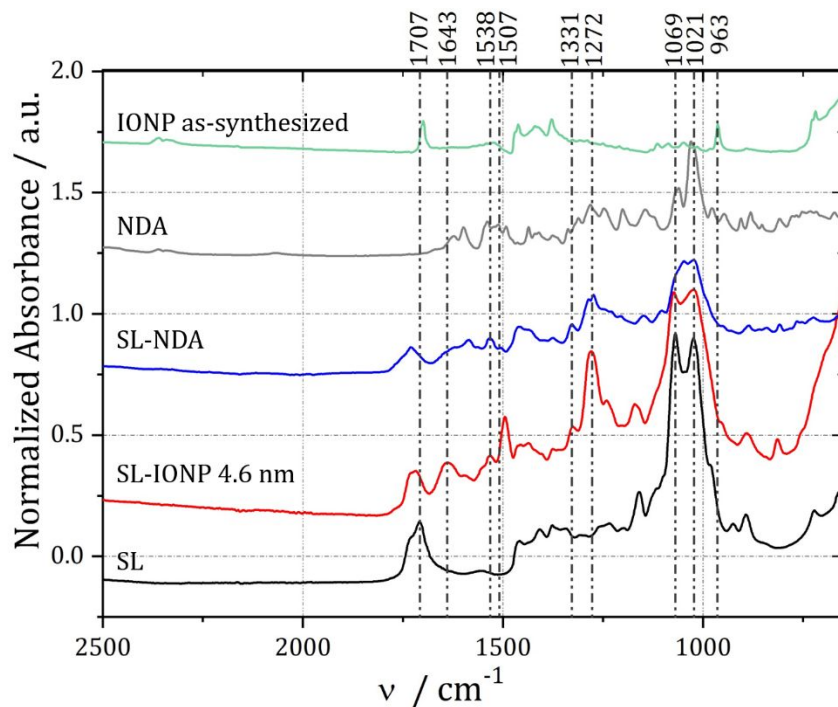


Figure 2 ATR-FTIR spectra of as-synthesized IONP (oleic acid capped, green), nitrodopamine (grey), sophorolipid-NDA (blue), SL-IONP 4.6 nm (red) and sophorolipid (black). Curves have been shifted vertically for clarity. With attributions: $\delta_{(C=O)-OH}$ (oleic acid): 963 cm^{-1} , ν_{C-O} (sugar): 1021 and 1069 cm^{-1} , ν_{C-O} (catechol): 1272 cm^{-1} , $\nu_s(\text{NO}_2)$: 1331 cm^{-1} , ν_{C-C} (catechol): 1507 cm^{-1} , $\nu_a(\text{NO}_2)$: 1538 cm^{-1} , $\nu_{C=O}$ (amide): 1643 cm^{-1} , $\nu_{C=O}$ (amide) and δ_{N-H} (amide): 1538 cm^{-1} and , $\nu_{C=O}$ (carboxylic): 1707 cm^{-1} .⁴¹⁻⁴³

1
2
3
4 The average grafting density of SL-NDA ligand irreversibly bound to the Fe-ions at the
5
6
7 IONP surface was evaluated after purification by TGA. Typical TGA weight loss profiles
8
9
10 for 3.1 nm SL-IONP, 4.6 nm SL-IONP and 14.1 nm SL-IONP are shown in Figure S4. The
11
12
13 total organic content (TOC) was determined as the fraction of mass loss up to 650 °C. If
14
15
16
17 all excess ligand is removed, the TOC can be converted into the dispersant grafting
18
19
20
21 density using the known molecular weight of SL-NDA, the defined average iron oxide core
22
23
24 area determined by TEM and a known iron oxide core density of 5.17 g/cm³. We thus
25
26
27
28 assume for this calculation that all oleic acid was replaced by SL-NDA during the rigorous
29
30
31
32 ligand replacement and purification. Earlier studies have shown that ligand replacement
33
34
35 of OA by hydrophobic ligands is challenging and can leave significant residues within the
36
37
38 nanoparticle shell.^{32, 44} If this is the case, the amount of SL-NDA grafted to the IONP
39
40
41
42 would be overestimated. However, we have previously investigated the ligand
43
44
45 replacement and purification protocol used here and shown that the amount of residual
46
47
48
49 OA is below the detection limit by ATR-FTIR. As discussed above, the ATR-FTIR data
50
51
52 shown in Figure 2 supports this finding. Additionally, the calculation of the grafting density
53
54
55
56 based on the TGA data can yield a higher value than the actual grafting density if there
57
58
59
60

1
2
3 is also free ligand present in a sample. We therefore list the average number of ligands (
4
5
6
7 $n_{ligands}$) per nm^2 in Table 2 calculated in the same way for differently sized IONP purified
8
9
10 by dialysis or membrane centrifugation (Amicon 50 kDa MWCO) to take into account the
11
12
13
14 possible presence of free ligand.
15
16
17
18
19
20
21

22 **Table 2.** TGA results for SL-IONP of three different core sizes. Total organic contents
23
24
25 (TOC) was converted into average number of ligands/ nm^2 ($n_{ligands}/\text{nm}^2$) using the known
26
27
28 SL-NDA Mw (902 g/mol).
29
30
31
32

SL-IONP type	$n_{ligands}/\text{nm}^2$ [dispersant/ nm^2]	TOC [%w/w]
3.1 ± 0.3 nm dialyzed	8.0 ^a	82.3 ^a
3.1 ± 0.3 nm Amicon	7.1 ^a	80.5 ^a
4.6 ± 0.3 nm dialyzed	4.3	60.8
4.6 ± 0.3 nm Amicon	3.3	55.6
14.1 ± 0.9 nm dialyzed	37.4 ^a	82.1 ^a

1
2
3
4 14.1 ± 0.9 nm
5 Amicon
6
7
8 45.2^a
9 84.8^a

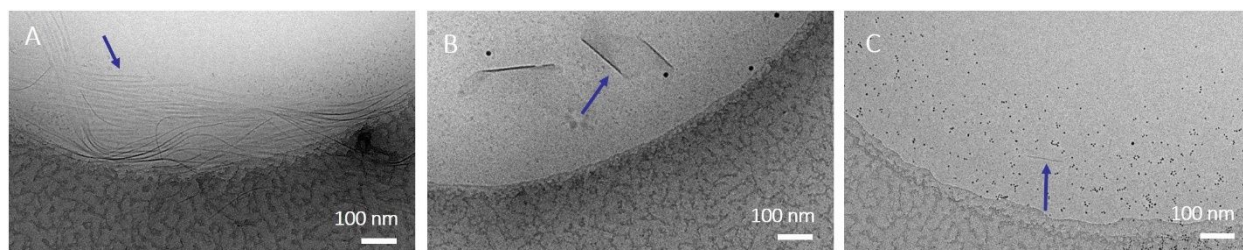
^a Samples contained large amounts of excess ligand.

10
11
12
13
14 The limiting factor for ligand adsorption to the IONP surface is given by the number of
15
16
17 surface iron sites (3.5 - 5.9 depending on crystal plane)⁴⁵ or the spatial requirements
18
19
20 (footprint) of the ligand. The hydrated sugar headgroup and the unsaturated fatty acid
21
22
23 structure of SL could sterically hinder achieving the maximum grafting density of NDA,
24
25
26 but this steric blocking is reduced by the high curvature of the IONP that provides much
27
28
29 larger volume for the headgroup than for the binding group. The grafting density of the
30
31
32 deacetylated acidic form of sophorolipids (the same used in this work) varies according
33
34
35 to the system under study; one finds between 2 and 3 molecules/nm² on a flat gold
36
37
38 surface (evaluated by X-ray photoelectron spectroscopy and quartz crystal microbalance
39
40
41 with dissipation monitoring),⁴⁶ 0.96 molecules/nm² at the air/water interface (surface
42
43
44 tension)⁴⁷ and between 0.5 and 1.0 molecules/nm² in micelles respectively at the
45
46
47 micelle/water and alkyl/sophorose interface (evaluated by SAXS).²⁰ The SL-IONP with a
48
49
50 diameter of 4.6 nm purified by Amicon have a ligand density of 3.3 molecules/nm², which
51
52
53
54
55
56
57
58
59
60

1
2
3 is within the range of plausible grafting densities taking both the density of grafting sites
4
5
6 and steric blocking during grafting into account. The other systems display values of SL-
7
8
9
10 NDA/nm² that are higher than the number of possible grafting sites on the IONP surface,
11
12
13 which sets an absolute upper bound on the grafting density. Hence, the observed values
14
15
16 above 5 molecules/nm² (Table 2) must be due to excess ligand that is not grafted to the
17
18
19
20 IONP surface. The excess ligand could not be removed with Amicon filters and dialysis
21
22
23
24 could also not reduce the organic content of the samples. It has been reported that
25
26
27
28
29
30
31
32
33
34
35
36
37
38
39
40
41
42
43
44
45
46
47
48
49
50
51
52
53
54
55
56
57
58
59
60
sophorolipids form micellar structures in water,²⁰ and cryo-TEM micrographs in Figure 3A
and Figure S5 demonstrate that also SL-NDA self-assembles into both spherical and
filamentous structures. Since it is not a goal of this work to describe the self-assembly
properties of SL-NDA in water, we prefer not to go into descriptive details; we will simply
refer to a general micellar and filamentous self-assembled phase of SL-NDA in
coexistence with SL-IONP.

Figures 3B-C and Figures S6 and S7 show cryo-TEM images of 14.1 and 4.6 nm SL-
IONP purified by membrane centrifugation. The 14.1 nm cores have the highest organic
content according to TGA, while the 4.6 nm cores have an organic content compatible

1
2
3 with maximum grafting of SL-NDA to the IONP surface. In addition to the nicely dispersed
4
5
6
7 SL-IONP with high electron density contrast, large and elongated structures with lower
8
9
10 contrast are present primarily in the 14.1 nm core sample; these strongly resemble the
11
12
13
14 filamentous structures formed by SL-NDA in water, depicted in Figure 3A.
15
16
17
18
19



30
31 **Figure 3.** Cryo-TEM micrographs in H₂O of A) SL-NDA, B) 14.1 nm SL-IONP and C) 4.6
32
33
34 nm SL-IONP. The blue arrows indicate lamellar structures formed by excess ligand; the
35
36
37 black dots are nanoparticles (see Figure S6 and S7 for enlarged pictures).
38
39
40
41
42
43
44
45

46 This feature suggests why SL-NDA could not be fully removed by dialysis or by
47
48
49 membrane centrifugation: the cut-off pore size of the membranes is larger than a single
50
51
52
53 SL-NDA molecule, but smaller than their self-assembled phase. Dialysis should in
54
55
56
57
58
59
60

1
2
3 principle allow for removal of excess lipid from the sample, but in practice, self-
4
5
6
7 aggregating molecules with a low critical aggregation constant or very slow kinetics of
8
9
10 desorption (low k_{off}) will make dialysis very inefficient; this is apparently the case for
11
12
13 dialysis of SL-NDA forming large and stable structures. An attempt to improve the dialysis
14
15
16
17 with salt (NaCl) by shifting the critical micelle concentration failed for this system since
18
19
20
21 SL-NDA micelles are insensitive to salt (*cf.* SANS data below). Interestingly, the small
22
23
24 core sample (4.6 nm) had much less excess ligand after purification than the large core
25
26
27
28 sample. This could tentatively be explained by that for the larger cores a larger excess of
29
30
31 SL-NDA to IONP surface area was used, which favors growth of more and larger micelles
32
33
34 during grafting or during resuspension. The 4.6 nm SL-grafted IONP presumably had a
35
36
37
38 lower amount of excess SL-NDA in solution after grafting and consequently a negligible
39
40
41
42 excess of SL-NDA in the dispersion after purification. This interpretation of the purification
43
44
45 and TGA data is supported by cryo-TEM (Figure 3C and Figure S7), in which many
46
47
48
49 stabilized nanoparticles are observed, but only a limited amount of SL-NDA. With the
50
51
52
53 difficulty to purify nanoparticles from SL-NDA micelles and filaments, one can try to
54
55
56 minimize the excess of SL-NDA during grafting to suppress micelle formation. However,
57
58
59
60

1
2
3 this easily leads to inefficient grafting and sub-monolayer dispersant grafting density on
4
5
6
7 the particle surface. Grafting with large SL-NDA excess is therefore recommended for
8
9
10 applications where excess micelles can be tolerated but particle colloidal stability is of
11
12
13
14 paramount importance.
15
16
17
18
19
20

21 **Characterization of the SL-NDA ligand shell with SANS and SAXS.** It is typically
22
23
24 assumed that the high colloidal stability of coated nanoparticles is explained by the
25
26
27 presence of a single layer of ligand; this argument may also hold for the SL-IONP
28
29
30 presented here. However, most classical techniques, like DLS or TEM, on which this
31
32
33
34 assumption is based, are generally not providing *in situ* or detailed enough data to
35
36
37
38 quantitatively investigate the presence, structure and properties of the shell in support of
39
40
41 this hypothesis. SAXS, which is sometimes used for this purpose, is mostly not suitable
42
43
44
45 for hybrid inorganic-organic nanoparticles, because the contrast between the solvent and
46
47
48 the electron-rich inorganic core generally masks the signal of the shell resulting from the
49
50
51
52 poor contrast between the solvent and the shell. The combined use of X-ray and neutron
53
54
55
56 scattering is the only method to probe the structural characteristics such as the thickness
57
58
59
60

1
2
3 of the nanoparticle organic shell. In fact, neutrons, being scattered by the atom nuclei,
4
5
6
7 are less sensitive to atoms with high atomic number. We therefore combined SAXS and
8
9
10 SANS as a reliable method to estimate the extension of the SL-NDA shell for SL-IONP
11
12
13
14 purified by Amicon filtration, that had a low excess of ligand in micelles.
15
16

17 SAXS was used to determine and confirm the size of the IONP cores. Under X-ray
18
19
20 irradiation, the inorganic core of SL-IONP nanoparticles has a very high contrast ($\rho_{solv} -$
21
22
23 $\rho_c = -30.60 \times 10^{-6} \text{ \AA}^{-2}$, Table 3) if compared to the shell-solvent ($\rho_{solv} - \rho_s = -0.57 \times 10^{-6}$
24
25
26 \AA^{-2} , Table 3); for this reason, SAXS only provides structural information on the
27
28
29
30
31 nanoparticle cores. Figure 4A (green circles) shows the SAXS profile for 4.6 nm SL-IONP.
32
33
34
35 The best fit using a core-shell sphere form factor can be obtained using an average
36
37
38 nanoparticle core diameter of 4.8 ± 0.4 nm and a null value for the shell thickness. This
39
40
41
42 is in very good agreement with the diameter obtained by TEM (4.6 ± 0.3 nm) within the
43
44
45 experimental errors. The corresponding SANS pattern (Figure 4A, blue circles) is shifted
46
47
48
49 towards the low- q region, which signifies sensitivity to the larger size resulting from the
50
51
52
53 much higher contrast of neutrons to the lipid shell.
54
55
56
57
58
59
60

1
2
3 The SANS pattern can be modeled using an imposed (from SAXS data) core diameter
4
5
6
7 of $d = 4.8 \pm 0.4$ nm and a shell thickness of $t = 2.5 \pm 0.2$ nm obtained by fitting a core-
8
9
10 shell model to the scattering data. This simple model assumes a uniform scattering length
11
12
13 density throughout the shell, which is clearly a simplification, but it can be used to estimate
14
15
16 the shell thickness by fitting the shift of the first minimum of the form factor. The calculated
17
18
19 length of SL, considering the 120° angle due to the mono-unsaturation, can be estimated
20
21
22 to 2.6 nm, where 1.6 nm are attributed to the fatty acid⁴⁸ and 1 nm to sophorose, in
23
24
25 analogy to the size of maltose, a common disaccharide.⁴⁹ The size of NDA is estimated
26
27
28 to about 1 nm.⁵⁰ Under these conditions, the maximum expected size for SL-NDA is about
29
30
31 3.6 nm. The modeled thickness of $t = 2.5 \pm 0.2$ nm is shorter than the maximum
32
33
34 monolayer thickness and demonstrates that the shell of monodisperse SL-IONP is
35
36
37 comprised of a single layer of SL-NDA of less than maximum density. From the fit, one
38
39
40 can also evaluate an average shell scattering length density of $\rho_s = 3.39 \times 10^{-6} \text{ 10}^{-6} \text{ \AA}^{-2}$, a
41
42
43 value which is reasonable for a hydrated (in D_2O) organic lipid layer.⁵¹ The lower density
44
45
46 or slightly lower thickness that is observed can be explained in several ways. One can,
47
48
49 e.g., consider that the shell could contain other smaller ligands than SL-NDA, such as
50
51
52
53
54
55
56
57
58
59
60

1
2
3 residual catalyst (COMU), oleic acid or unreacted NDA or SL. The combination of TGA,
4
5
6
7 FTIR and NMR data make this hypothesis unlikely. COMU, which was observed as
8
9
10 residue in the SL-NDA batches used for grafting the NPs, has very low affinity for the iron
11
12
13 oxide surface. All techniques employed show no evidence of residual OA, while ¹H NMR
14
15
16 shows that the SL-NDA does not contain free NDA. A residual amount of unreacted SL
17
18
19 (10-20 mol% with respect to SL-NDA) is present. The carboxyl endgroup of SL has high
20
21
22 affinity to the IONP, but NDA functionalized ligands possess much higher affinity and
23
24
25 outcompete carboxyl anchored ligands on the surface. This is demonstrated by FTIR
26
27
28 showing the successful ligand replacement of OA by SL-NDA and previous studies of e.g.
29
30
31
32
33
34
35
36
37
38
39
40
41
42
43
44
45
46
47
48
49
50
51
52
53
54
55
56
57
58
59
60

OA with SL failed to produce water-soluble particles, strongly suggesting that replacement of OA will be driven by SL-NDA. Thus, although our data do not allow its exclusion, we do not expect significant amounts of unmodified SL on the IONP.

A more plausible explanation for the thin shell is that the SL-NDA is grafted on a highly curved surface, which provides a rapidly increasing conical volume to the SL-NDA even at the highest grafting density.⁵² This allows for a large tilt or bending of the molecules,

1
2
3 i.e. a lower effective shell thickness. The extended length of SL is calculated according
4
5
6
7 to the classical Tanford formula. However, SL is known to adopt a bent configuration,
8
9
10 which yields an effectively thinner layer than theoretically calculated. For instance, XPS
11
12
13 has shown that a single self-assembled monolayer of cysteamine-modified SL grafted
14
15
16 onto flat gold has a thickness of only 3.0 ± 0.2 nm,⁴² while small-angle X-ray and neutron
17
18
19 scattering measurements showed that the total radius of an acidic SL micelle is generally
20
21
22 below 4 nm, i.e, approximately the size of a single SL molecule.⁵³⁻⁵⁴ A layer grafted on a
23
24
25 highly curved NP would be expected to yield a thickness in between these estimates.
26
27
28
29
30

31 Finally, one should not exclude that the simplification of assuming a uniform scattering
32
33
34 length density, which could be invalidated by the conical ligand volume and the highly
35
36
37 hydrated headgroup, would also lead to a fit predicting an effectively thinner shell.
38
39
40
41 Whichever the dominant of the two latter explanations, the SAXS/SANS data demonstrate
42
43
44
45 a single thin SL-NDA layer serving as the stabilizing shell on the IONP.
46
47
48
49
50
51
52
53
54
55
56
57
58
59
60

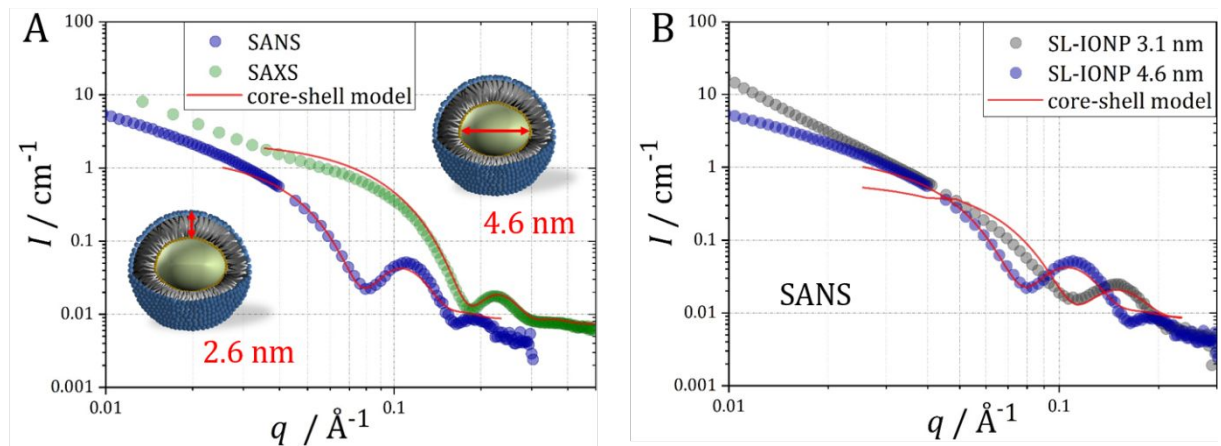


Figure 4. A) SANS (blue) and SAXS (green) profiles for 4.6 nm SL-IONP in D_2O . The red lines show the fit obtained from a core-shell sphere model. The best fit for SAXS was obtained using a core diameter of 4.8 nm and a null value for the shell. B) Comparison of the SANS data of 4.6 nm (blue) and 3.1 nm SL-IONP (grey). As expected, the profile for smaller SL-IONP is shifted to larger q . The red lines show the fit obtained with a homogeneous core-shell model.

Similar results are obtained for the smaller 3.1 nm SL-IONP (Figure 4B). The SANS pattern can be modelled with a fixed (from SAXS data) core diameter, $d = 3.0 \pm 0.2$ nm and a fitted shell thickness of $t = 2.2 \pm 0.2$ nm. These data are summarized in Table 3,

which also contains the solvent-core and solvent-shell scattering length density contrasts fitted from the SANS data: $\rho_{solv} - \rho_c = -0.57 \times 10^{-6} \text{ \AA}^{-2}$ while $\rho_{solv} - \rho_s$ is in the order of $3.0 \times 10^{-6} \text{ \AA}^{-2}$. This demonstrates that the shell has higher contrast than the iron oxide core, and therefore dominates the scattering signal of the core-shell particle. The absolute value of the shell scattering length density for 3.1 nm SL-IONP is $\rho_s = 3.45 \times 10^{-6} \text{ \AA}^{-2}$ and in good agreement with what is found for the 4.6 nm core SL-IONP.

Table 3. Structural parameters for the 3.1 nm and 4.6 nm SL-IONP obtained by combining TEM, SAXS and SANS analyses.

Sample	Technique	Core diameter d (nm)	Shell Thickness t (nm)	$\rho_{solv} - \rho_c$ ($\times 10^{-6} \text{ \AA}^{-2}$)	$\rho_{solv} - \rho_s$ ($\times 10^{-6} \text{ \AA}^{-2}$)
3.1 nm SL-IONP	TEM	3.1 ± 0.2	-	-	-
	SAXS	3.0 ± 0.4	-	-30.60	< -1.00
	SANS	3.0 ± 0.4	2.5 ± 0.2	-0.57	2.63
4.6 nm SL-IONP	TEM	4.6 ± 0.2	-	-	-
	SAXS	4.8 ± 0.4	-	-30.60	< -1.00
	SANS	4.8 ± 0.4	2.2 ± 0.2	-0.57	3.00

1
2
3
4
5
6
7
8
9
10 The scattering curve of the 14.1 nm SL-IONP sample was radically different to those of
11
12 the dispersions of the two smaller SL-grafted IONP and is shown in Figure 5. The typical
13
14 SANS spectrum for 14.1 nm SL-IONP in D₂O (blue filled circles) is relatively featureless
15
16 in D₂O, but it shows strong scattering with a characteristic slope in the low- q region that
17
18 is not present in the SANS spectra of the smaller SL-grafted IONP. This additional feature
19
20 can be explained by comparing the data to the SANS spectrum of the pure SL-NDA ligand
21
22 solution (Figure 5, grey filled circles), which nicely matches the spectrum of the 14.1 nm
23
24 SL-IONP sample. Thus, in good agreement with the TGA data presented in Figure S4
25
26 and Table 2, the SANS signal of the 14.1 nm SL-IONP dispersion is dominated by SL-
27
28 NDA in the form of filamentous structures instead of the core-shell particles. The higher
29
30 contrast of SL-NDA to D₂O than of iron oxide to D₂O further contributes to the dominance
31
32 of scattering from the SL-NDA micelles. These micelles were also prevalent in cryo-TEM
33
34 images of the 14.1 nm SL-IONP sample (see Figure 3B). Nonetheless, SL-NDA is soluble
35
36 in perdeuterated methanol, as shown by the corresponding poor SANS signal (grey empty
37
38
39
40
41
42
43
44
45
46
47
48
49
50
51
52
53
54
55
56
57
58
59
60

1
2
3
4 circles) in Figure 5 5. As expected, the SANS pattern of 14.1 nm SL-IONP (blue empty
5
6
7 circles) in MeOD-d4 loses the SL-NDA scattering profile and it rather presents the typical
8
9
10 feature of spherical objects. A shell-free 14.1 nm diameter IONP nanoparticle would be
11
12
13
14 expected to have the first minimum of the form factor around $q = 0.4 \text{ nm}^{-1}$, whereas the
15
16
17 minimum of the oscillation of the form factor measured for the 14.1 nm SL-IONP falls
18
19
20
21 between $0.2 \text{ nm}^{-1} < q < 0.3 \text{ nm}^{-1}$, suggesting a spherical object sized between 20 and 30
22
23
24 nm. This is largely in agreement to what would be expected for a 14.1 nm iron oxide core,
25
26
27 stabilized by a single SL-NDA layer even if the conditions of analysis (excess of SL-NDA,
28
29
30
31 methanol) and likely presence of aggregates do not allow the quantification of the
32
33
34
35 thickness of the SL-NDA layer.
36
37
38
39
40
41
42
43
44
45
46
47
48
49
50
51
52
53
54
55
56
57
58
59
60

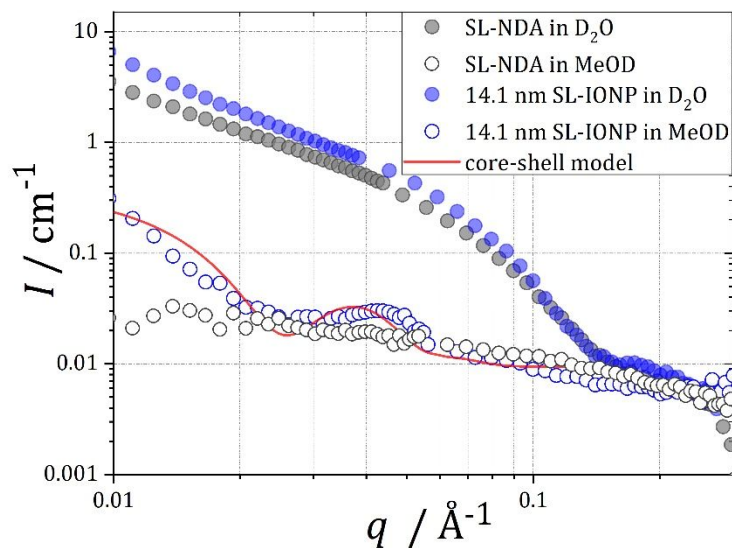


Figure 5. SANS data recorded for 14.1 nm SL-IONP in D_2O (blue filled circles) and MeOD-d4 (blue empty circles) and the pure ligand SL-NDA in D_2O (grey filled circles) and MeOD-d4 (grey empty circles).

Colloidal stability and long-term stability. Removal of all monomeric free SL-NDA, is a good test of the colloidal stability of SL-NDA-grafted IONP. However, a biological environment is much more challenging for IONP colloidal stability, due to the higher concentration of biological colloids, displaying a larger variety of attractive interactions and leading to nanoparticle aggregation.⁵ Thus, colloidal stability of nanoparticles meant

1
2
3 to perform functions in biotechnological or medical applications should be tested under
4
5
6
7 conditions where they are exposed to full physiological ionic strength as well as to
8
9
10 concentrations of protein similar to those that could be encountered during application.

11
12
13
14 Therefore, we suspended the SL-IONP in 10 % fetal calf serum (FCS), which has a lower
15
16
17 concentration than full serum, but at which the colloidal stability can be monitored by DLS.

18
19
20
21 10 % serum also corresponds to the typical additive to cell culture media. We performed
22
23
24 the measurements while heating from 20 °C to 70 °C and back. These conditions are
25
26
27 known to weaken the hydration of the nanoparticle shell⁵⁵ and thereby reduce the colloidal
28
29
30 stability and decrease the ability to suppress adsorption of serum protein. Adsorption of
31
32
33 denatured proteins leads to irreversible aggregation and precipitation of insufficiently
34
35
36 stabilized nanoparticles⁵⁶. Figure 6 shows the evolution of the volume weighted
37
38
39 hydrodynamic diameter D_H of 4.6 nm SL-IONP in water with 10 % FCS with temperature.
40
41
42
43
44

45
46 Volume weighed D_H of 4.6 nm SL-IONP in water is shown in Figure S8A. The
47
48
49 hydrodynamic diameter of 4.6 nm SL-IONP was measured to be around 12 nm, which
50
51
52 was stable after more than 1.5 years in storage. The SL-IONP with 3.1 nm and 14.1 nm
53
54
55 core sizes appeared equally stable in dispersion over the same time period. However, the
56
57
58
59
60

1
2
3 stability could not be quantitatively confirmed by the hydrodynamic diameter, as there
4
5
6 were excess SL-NDA in these samples. All investigated SL-IONP have small diameters
7
8
9
10 in the superparamagnetic range and they are stabilized predominantly by steric and
11
12
13 hydration forces from the hydrophilic headgroup region of the sophorolipid. It is
14
15
16 advantageous for many applications to have a thin stabilizing shell of this kind to reduce
17
18
19 the overall hydrodynamic size. However, we note that the strength of the long-range
20
21
22 attractive van der Waals forces increases if the inorganic nanoparticle core is made
23
24
25 larger. It is likely that there is a maximum core size for which an SL-NDA shell can provide
26
27
28 sufficient stabilization against aggregation by dipolar interactions.
29
30
31
32
33

34
35 The hydrodynamic diameter of the 4.6 nm SL-IONP is in reasonable agreement with
36
37
38 the size of the core-shell nanoparticle determined by SANS, ~9.2 nm, which might
39
40
41 underestimate the steric or hydrodynamic size due to the fitting of a homogeneous shell.
42
43
44
45 The DLS result is also in good agreement with a theoretical size of a core-shell IONP
46
47
48 calculated from the diameter of the core measured by TEM (4.6 nm) and the length of a
49
50
51 SL-NDA molecule (3 nm), which implies a total steric diameter of 10.6 nm diameter. Thus,
52
53
54
55 both DLS and SANS data strongly suggest a monolayer of SL-NDA ligands on the NP
56
57
58
59
60

1
2
3 surface. The size distribution measured for the monodisperse iron oxide nanoparticles
4
5
6
7 grafted with SL-NDA is narrower and with a smaller D_H than the SL-coated iron oxide
8
9
10 nanoparticles reported in our earlier work.²⁶ This is attributed to the novel synthesis
11
12
13
14 protocol with improved ligand and anchor chemistry for grafting to monodisperse iron
15
16
17
18
19
20
21
22
23
24
25
26
27
28
29
30
31
32
33
34
35
36
37
38
39
40
41
42
43
44
45
46
47
48
49
50
51
52
53
54
55
56
57
58
59
60

surface. The size distribution measured for the monodisperse iron oxide nanoparticles grafted with SL-NDA is narrower and with a smaller D_H than the SL-coated iron oxide nanoparticles reported in our earlier work.²⁶ This is attributed to the novel synthesis protocol with improved ligand and anchor chemistry for grafting to monodisperse iron oxide core particles. Volume weighted D_H size distributions of 10 % FCS in Milli-Q without nanoparticles measured at 20 °C and 70 °C are shown in Figure S8B. The size of serum proteins was measured to be ~5 nm at 20 °C. A size shift to 8 nm was observed at elevated temperatures.

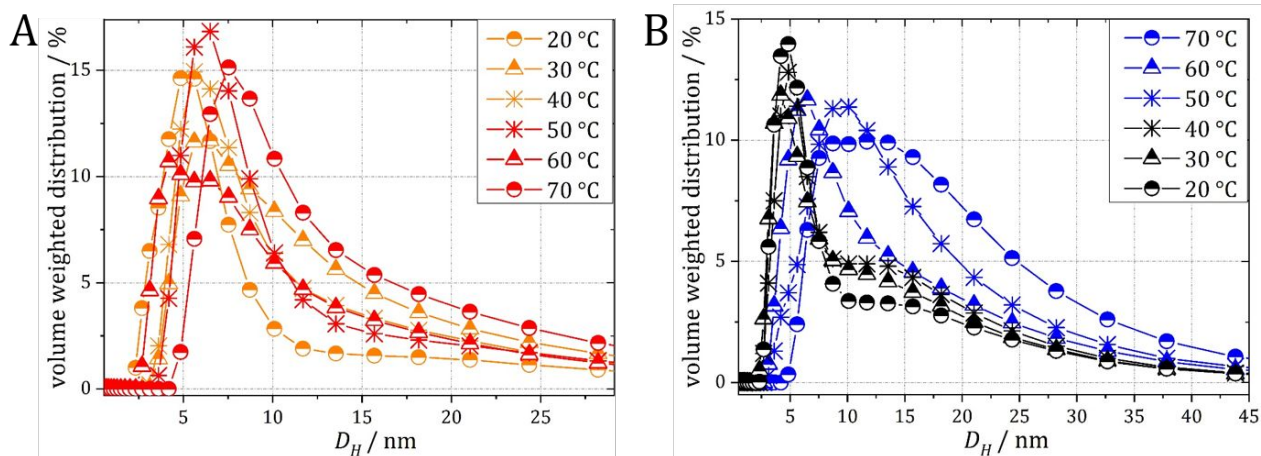


Figure 6. Volume weighted hydrodynamic diameters D_H of 4.6 nm SL-IONP dispersed in water with 10 % FCS heated from A) 20 °C to 70 °C and B) cooled from 70 °C to 20 °C with 3 minutes equilibration time at each temperature.

1
2
3
4
5
6
7
8 When heating up the SL-IONP in FCS, we observed a size distribution with the main
9
10
11 peak corresponding to the abundant serum albumin, with a tail towards larger sizes
12
13
14 contributed by the SL-IONP. Upon heating, the fraction of small objects (serum albumin)
15
16
17 in the size distribution decreased and the volume fraction of larger objects (nanoparticles)
18
19
20 increased. This results from partial denaturation and aggregation of serum proteins. This
21
22
23 trend becomes even more obvious in Figure 6B where a temperature of 70 °C was held
24
25
26 for 8 minutes to allow for more equilibration of the sample. Here, the apparent volume
27
28
29 fraction of nanoparticles is even larger, which could be due to precipitation of serum
30
31
32 protein. Importantly, no aggregation and precipitation of SL-IONP was observed at any
33
34
35 temperature, with or without exposure to denatured serum protein. This can also be
36
37
38 observed from the intensity weighted size distributions for the same temperature cycling
39
40
41 experiment (Figure S11). Figure S9 shows a photograph of SL-IONP after temperature
42
43
44 cycling. Aggregation of SL-IONP could not be induced by heating the samples in FCS at
45
46
47 70 °C for 3 h (Figure S10). Similar to the observations during temperature cycling, only a
48
49
50
51
52
53
54
55
56
57
58
59
60

1
2
3 small shift in size is observed after heating for 3 h and a very small peak in the intensity
4
5
6
7 weighted D_H appears at large sizes, indicating the aggregation of the protein that
8
9
10 precipitated after 3 h heating (Figure S12). These data, showing the excellent stability of
11
12
13 SL-IONP with temperature, can be explained by the small influence that temperature has
14
15
16
17 on the dehydration of the carbohydrate moiety of sugar-based capping agents. Sugar-
18
19
20 based dispersants are both hydrogen-bond donors and acceptors, which allows for a bulk
21
22
23 water-like hydrogen-bonding network and thereby low sensitivity to dehydration upon
24
25
26
27 increasing temperature.
28
29
30

31 The excellent colloidal stability of the SL-IONP nanoparticles is further demonstrated by
32
33
34 additional experiments performed in the presence of 1 M NaCl in D_2O . The high ionic
35
36
37 strength of 1 M NaCl was chosen for the ability of the NaCl ions to screen and reduce
38
39
40 double layer repulsion, thereby increasing the propensity of nanoparticles to aggregate,
41
42
43 as well as the ability of the mild kosmotropes to reduce hydration and thereby decrease
44
45
46 stabilization due to steric and hydration forces. Figure 7 presents the typical SANS
47
48
49 spectra for the 3.1 nm and 4.6 nm SL-IONP in 1 M NaCl D_2O in comparison with SL-IONP
50
51
52
53
54
55
56 in pure D_2O .
57
58
59
60

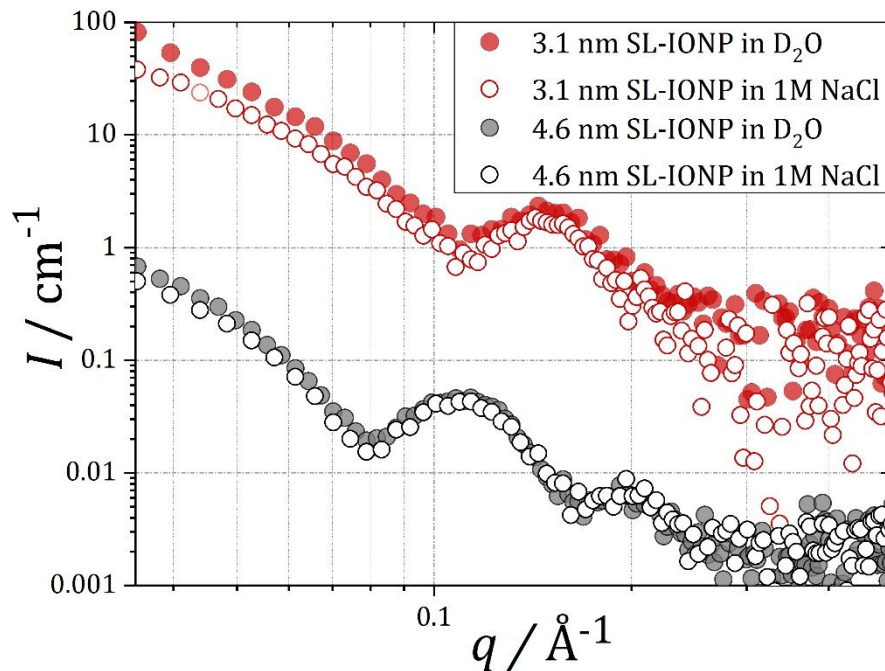


Figure 7. SANS data recorded for 3.1 nm and 4.6 nm SL-IONP in D_2O (red and grey filled circles respectively) and in 1 M NaCl (dissolved in D_2O) (red and grey empty circles respectively).

The data show that the SANS profiles of neither sample change when the ionic strength of the solvent is increased. The absence of change is true in both the mid/high- q region characteristic of the core-shell structure and in the low- q region characteristic of aggregation. This indicates that the SL-NDA shell has neither been removed upon salt addition, nor has its structure been modified. This contrasts to previous findings for

1
2
3
4
5
6
7
8
9
10
11
12
13
14
15
16
17
18
19
20
21
22
23
24
25
26
27
28
29
30
31
32
33
34
35
36
37
38
39
40
41
42
43
44
45
46
47
48
49
50
51
52
53
54
55
56
57
58
59
60

sophorolipid coated nanoparticles, where aggregation was promoted by the addition of salt.²⁶ The improved stability of our novel SL-IONP can be attributed to the NDA anchor chemistry that irreversibly grafts the SL coating densely to the cores. Furthermore, the SANS profiles do not show any sign of particle aggregation, since a structure factor corresponding to particle aggregation would appear in the low q -range. There is also no optically visible increase in scattering nor does precipitation take place, which supports the SANS observation of excellent colloidal stability. This is in full agreement with the DLS data that showed retained size and no aggregation and precipitation (*cf.* Figure 6). The SANS measurements also show that micelles of excess ligand in the 3.1 nm SL-IONP sample were not altered by that addition of salt (no change in the slope at low q), which explains why dialysis at high ionic strength could not remove the excess ligand.

***In-vitro* cellular uptake and cytotoxicity of SL-IONP.** To prove the applicability of SL-IONP in the biomedical field, we conducted cellular uptake and cytotoxicity tests on two different cell lines: U937 monocytes which are part of the reticuloendothelial system and

1
2
3 responsible for clearance of pathogens and foreign bodies from the blood and MCF7, a
4
5
6
7 human breast cancer cell line.
8
9

10 Differentiated monocytes, macrophages, are the cells in the body that are most exposed
11
12
13
14 to toxins and foreign bodies. The response of these cells to exposure of SL-IONP is thus
15
16
17 of highest relevance. If they detect and scavenge nanoparticles, the nanoparticles will be
18
19
20
21 of limited use in applications that require circulation and/or targeting. It is, to the best of
22
23
24 our knowledge, the first time that cellular uptake and toxicity are studied for sophorolipid
25
26
27 coated core-shell nanoparticles. Figure 8 shows the results of the cellular uptake and
28
29
30 cytotoxicity tests for 4.6 nm SL-IONP with U937 and MCF7 cells. SL-IONP show very low
31
32
33 non-specific uptake by both monocytes and cancer cells. A slight trend to higher uptake
34
35
36 of breast cancer cells over the phagocytic monocytes could not be statistically verified.
37
38
39
40
41 The low uptake is in the same order as previously shown for stealth poly(ethylene glycol)-
42
43
44 grafted IONP⁹ and can be traced back to the good colloidal stability of the core-shell SL-
45
46
47 IONP and their resistance against aggregation in presence of proteins and salts (*cf.*
48
49
50
51
52 Figure 6 and 7).
53
54
55
56
57
58
59
60

Both sphorolipids and iron oxide nanoparticles have individually shown negligible toxicity at relevant concentrations to various cell lines.⁵⁷⁻⁵⁸ Figure 8B shows that also SL-grafted 4.6 nm IONP do not affect the viability of the two tested cell lines. The results suggest an excellent biocompatibility of the SL-IONP.

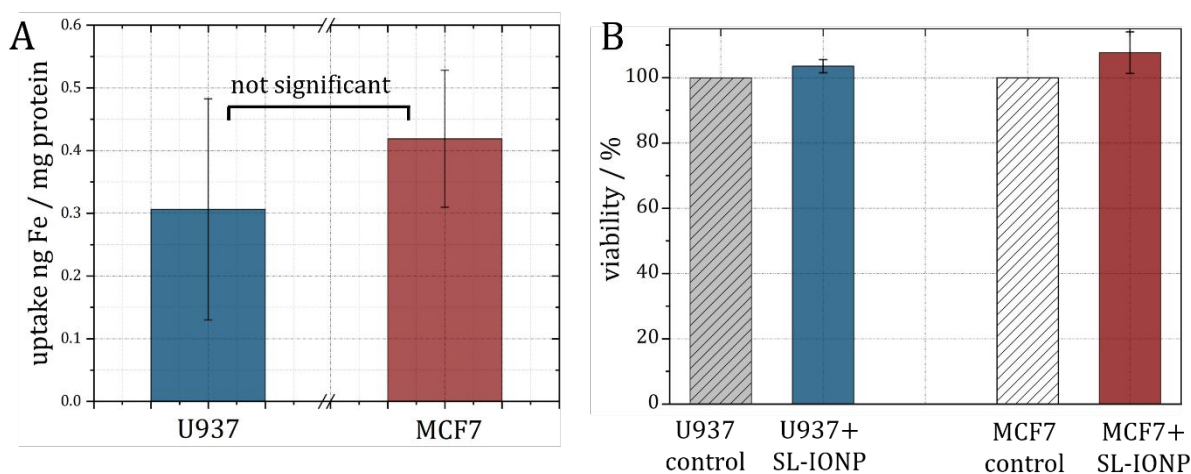


Figure 8. A) Cellular uptake of 4.6 nm SL-IONP for human monocytes (U937) and human breast cancer cells (MCF7). Negligible uptake was observed with a tendency towards increased uptake in cancer cell lines, but without statistical significance ($p > 0.05$ ANOVA 1-way) within the study. B) Cytotoxicity tests for 4.6 nm SL-IONP with human monocytes (U937) and human breast cancer cells (MCF7). The viability was unchanged for both cell lines.

1
2
3
4
5
6 **Design principles for using SL-NDA to stabilize IONP for applications.** In summary, a
7
8
9 range of challenging conditions for colloidal stability relevant for applications were tested;
10
11
12 all results were consistent with excellent stability of the grafted SL-NDA shell translating
13
14
15 to equally excellent colloidal stability. The low size dispersity, high grafting density and
16
17
18 colloidal stability of the SL-IONP system developed here are comparable to those of
19
20
21 synthetic glyconanoparticles^{12, 16-17, 59-60} rather than sophorolipid-capped nanoparticles.²³⁻
22
23
24
25
26
27 ²⁶ Our results demonstrate that the densely grafted SL-NDA shell provides a stable
28
29
30 repulsive potential preventing both mutual aggregation and protein adsorption under
31
32
33 highly challenging conditions (1 M NaCl, 70 °C with and without FCS). The colloidal
34
35
36 stability is not adversely affected by temperature and kosmotrope salts that often have a
37
38
39 destabilizing effect on polymer coated-core-shell nanoparticles. This is reached by the
40
41
42 irreversible grafting of the SL ligand to the core in contrast to pure self-assembly and/or
43
44
45 complexation. The expected main contribution to the repulsive interaction of the shell is
46
47
48 the high and stable hydration of the lipid head-groups that is apparently strong enough to
49
50
51 withstand weakening in the coordination of associated water under relevant challenging
52
53
54
55
56
57
58
59
60

1
2
3 environmental conditions. This fact is confirmed by the literature on the micellization
4
5
6
7 properties of sugar-based amphiphiles: the strength between the hydrogen bonding
8
9
10 between the hydroxyl groups of the sugar unit and water is stronger than between
11
12
13
14 ethylene oxide and water.⁶¹
15
16

17 It is worth noting that stabilization through a grafted lipid is fundamentally different to
18
19
20 the more commonly applied approach of a high- M_w flexible polymer; the low thickness
21
22
23 added by a lipid monolayer and its insignificant molecular flexibility makes it possible to
24
25
26
27 design such shells much more compact and structurally precise than using solvated
28
29
30
31 polymer. At the same time, it is impressive that equally high colloidal stability, as
32
33
34 demonstrated here, can be obtained. The hydrophobic spacer part of the lipid shell is
35
36
37
38 important to reduce core-core van-der-Waals attraction and likely cannot be made too
39
40
41 thin without compromising colloidal stability. However, with a hydrophobic interior of the
42
43
44 shell, a prerequisite for stability in biofluids is that the lipid shell (the lipid headgroup
45
46
47 region) is dense enough to prevent hydrophobic molecules, such as protein denatured by
48
49
50
51 temperature, to adsorb to shell defects exposing the alkyl part of the lipids. We achieved
52
53
54
55 this by the stable NDA-coupling and efficient ligand exchange protocol used to graft the
56
57
58
59
60

1
2
3 SL-NDA shell. As expected, in the absence of aggregates, the SL-IONP showed only
4
5
6
7 weak interaction with cells *in-vitro* with negligible uptake and no resulting cytotoxicity, thus
8
9
10 making these systems promising candidates for the development of IONP-based
11
12
13 biomedical applications. These, so-called stealth, nanoparticles can be further
14
15
16
17 functionalized or make use of specific interactions of the exposed saccharide motif to add
18
19
20 targeting capability, for which structural and colloidal stability, as well as suppression of
21
22
23 non-specific biomolecular interactions, is a prerequisite.
24
25
26
27
28
29
30

31 Conclusion

32
33
34 We have synthesized monodisperse, biocompatible, sophorolipid-grafted core-shell
35
36
37 iron oxide nanoparticles with excellent colloidal stability in demanding application
38
39
40 environments mimicking the conditions of biological fluids. As-synthesized, oleic acid-
41
42
43 coated IONP with precisely tunable sizes and narrow size distributions were successfully
44
45
46
47 grafted with a nitrodopamide-modified sophorolipid ligand by replacement of the oleic
48
49
50
51 acid. Analysis of TGA and cryo-TEM highlighted the challenge of removing excess ligand
52
53
54
55 as sophorolipid forms very stable aggregates of similar size as the grafted nanoparticles
56
57
58
59
60

1
2
3 and with the same physico-chemical characteristics. Cryo-TEM revealed the coexistence
4
5
6
7 of individual, monodisperse, SL-grafted IONP with large and stable SL-NDA aggregates
8
9
10 formed by excess ligand that could not be completely removed by excessive purification.
11
12
13
14 However, also close to pure SL-grafted IONP product was obtained for 4.6 nm IONP
15
16
17 cores. The core-shell structure of SL-IONP was analyzed by SAXS and SANS. The
18
19
20 resulting data were successfully fitted with a core-shell model. SANS revealed the
21
22
23
24 thickness of the shell, which was found to be in the order of 2.5 nm, in good agreement
25
26
27
28 with a shell composed of a monolayer of SL-NDA grafted to a highly curved surface.
29
30

31 The stable, grafted core-shell architecture presenting the equivalent of a dense
32
33
34 sophorolipid membrane at the nanoparticle surface was shown to translate into excellent
35
36
37
38 colloidal stability under demanding conditions such as in dense protein dispersions
39
40
41
42 (serum) at high temperature and at high ionic strength, as shown by DLS and SANS. The
43
44
45
46 resulting colloiddally stable and biocompatible SL-IONP are promising materials in the
47
48
49 biomedical field through their combination of IONP imaging and therapeutic properties
50
51
52
53 with natural presentation of functional glycosylation, whereas carbohydrate-rich
54
55
56
57
58
59
60

1
2
3 nanoparticles can display unique targeting ability towards lectin-rich biological
4
5
6
7 membranes, including tumor cells and pathogenic bacteria.
8
9
10
11
12
13
14

15 ASSOCIATED CONTENT

16
17
18

19 **Supporting Information.** Additional information on Materials. Control over iron oxide core
20
21
22 size by the precursor to surfactant ratio. Detailed synthetic protocols. NMR, IR, TGA,
23
24
25
26 TEM, cryo-TEM and DLS data for SL-NDA and SL-IONP. Photos of colloidal suspensions.
27
28
29
30 Additional SAXS and SANS data with fits.
31
32
33

34 AUTHOR INFORMATION

35
36
37

38 Corresponding Authors

39
40
41

42 *Erik Reimhult: erik.reimhult@boku.ac.at; Niki Baccile: niki.baccile@upmc.fr.
43
44
45

46 Author Contributions

47
48
49

50 AL, ER and NB planned the work. AL and NB performed most of the experiments. AL, ER
51
52
53 and NB wrote the manuscript. All authors contributed to and reviewed the manuscript.
54
55
56
57
58
59
60

1
2
3
4 The manuscript was written through contributions of all authors. All authors have given
5
6
7 approval to the final version of the manuscript.
8
9

10 11 **Funding Sources** 12

13
14
15 This work received financial support by the Institut Laue-Langevin (ILL), Grenoble,
16
17
18 France, under the experiment number 9-12-481 (D33, D16 beamlines), and by the
19
20
21 European Synchrotron Radiation Facility (ESRF), Grenoble, France, under the
22
23
24 experiment number SC-4419. The research presented in that paper was funded by the
25
26
27
28
29 Austrian Science Fund (FWF) project I 3064 and by the European Research Council
30
31
32 under the European Union's Seventh Framework Program (FP/2007-2013)/ERC Grant
33
34
35
36 Agreement No. 310034.
37
38
39

40 41 **ACKNOWLEDGMENT** 42

43
44
45 This work benefited from the use of the SasView application, originally developed under
46
47
48 NSF award DMR-0520547. SasView contains code developed with funding from the
49
50
51 European Union's Horizon 2020 research and innovation programme under the
52
53
54
55 SINE2020 project, grant agreement No 654000. We thank the Lawrence Berkeley
56
57
58
59
60

1
2
3 National Laboratory for access to TEM; work at the Molecular Foundry was supported by
4
5
6
7 the Office of Science, Office of Basic Energy Sciences, of the U.S. Department of Energy
8
9
10 under Contract No. DE-AC02-05CH11231. We thank Prof. Dieter Baurecht for access to
11
12
13
14 FTIR. We acknowledge the VIBT Extremophile Center for access to TGA.
15
16
17
18
19
20

21 ABBREVIATIONS

22
23 IONP, iron oxide nanoparticles; OA, oleic acid; Oct₂O, dioctylether; SL, sophorolipids;
24
25
26
27 NDA, nitrodopamine/nitrodopamide; SL-NDA, sophorolipid-nitrodopamide; SL-IONP,
28
29
30 sophorolipid-nitrodopamide-grafted iron oxide nanoparticles; PEG, poly(ethylene glycol);
31
32
33
34 PBS, Phosphate buffered saline; FCS, fetal calf serum; HR, high-resolution; LR, low-
35
36
37 resolution; TEM, transmission electron microscope/microscopy; TGA, thermogravimetric
38
39
40
41 analysis; DLS, dynamic light scattering; NMR, nuclear magnetic resonance; ATR-FTIR,
42
43
44 attenuated total reflection – Fourier transform infra-red; SAXS, small angle x-ray
45
46
47 scattering; SANS, small angle neutron scattering; SLD, scattering length density; MWCO,
48
49
50
51 molecular weight cut-off; TOC, total organic content
52
53
54
55
56
57
58
59
60

REFERENCES

1. Hong, R. Y.; Feng, B.; Chen, L. L.; Liu, G. H.; Li, H. Z.; Zheng, Y.; Wei, D. G., Synthesis, Characterization and MRI Application of Dextran-Coated Fe₃O₄ Magnetic Nanoparticles. *Biochem. Eng. J.* 2008, 42, 290-300.
2. Lacava, L. M.; Lacava, Z. G. M.; Da Silva, M. F.; Silva, O.; Chaves, S. B.; Azevedo, R. B.; Pelegrini, F.; Gansau, C.; Buske, N.; Sabolovic, D.; Morais, P. C., Magnetic Resonance of a Dextran-Coated Magnetic Fluid Intravenously Administered in Mice. *Biophys. J.* 2001, 80, 2483-2486.
3. Tassa, C.; Shaw, S. Y.; Weissleder, R., Dextran-Coated Iron Oxide Nanoparticles: A Versatile Platform for Targeted Molecular Imaging, Molecular Diagnostics, and Therapy. *Acc. Chem. Res.* 2011, 44, 842-852.
4. Boni, A.; Bardi, G.; Bertero, A.; Cappello, V.; Emdin, M.; Flori, A.; Gemmi, M.; Innocenti, C.; Menichetti, L.; Sangregorio, C.; Villa, S.; Piazza, V., Design and Optimization of Lipid-Modified Poly(Amidoamine) Dendrimer Coated Iron Oxide Nanoparticles as Probes for Biomedical Applications. *Nanoscale* 2015, 7, 7307-7317.
5. Amstad, E.; Textor, M.; Reimhult, E., Stabilization and Functionalization of Iron Oxide Nanoparticles for Biomedical Applications. *Nanoscale* 2011, 3, 2819-2843.
6. Frey, N. A.; Peng, S.; Cheng, K.; Sun, S., Magnetic Nanoparticles: Synthesis, Functionalization, and Applications in Bioimaging and Magnetic Energy Storage. *Chem. Soc. Rev.* 2009, 38, 2532-2542.
7. Park, J.; Joo, J.; Kwon, S. G.; Jang, Y.; Hyeon, T., Synthesis of Monodisperse Spherical Nanocrystals. *Angew. Chem. Int. Ed.* 2007, 46, 4630-4660.
8. Lassenberger, A.; Bixner, O.; Gruenewald, T.; Lichtenegger, H.; Zirbs, R.; Reimhult, E., Evaluation of High-Yield Purification Methods on Monodisperse Peg-Grafted Iron Oxide Nanoparticles. *Langmuir* 2016, 32, 4259-4269.
9. Lassenberger, A.; Scheberl, A.; Stadlbauer, A.; Stiglbauer, A.; Helbich, T.; Reimhult, E., Individually Stabilized, Superparamagnetic Nanoparticles with Controlled Shell and Size Leading to Exceptional Stealth Properties and High Relaxivities. *ACS Appl. Mater. Interfaces* 2017, 9, 3343-3353.

10. Yang, Q.; Lai, S. K., Anti-PEG Immunity: Emergence, Characteristics, and Unaddressed Questions. Wiley interdisciplinary reviews. Nanomed. Nanobiotechnol. 2015, 7, 655-677.
11. Bernardi, A.; Jimenez-Barbero, J.; Casnati, A.; De Castro, C.; Darbre, T.; Fieschi, F.; Finne, J.; Funken, H.; Jaeger, K.-E.; Lahmann, M.; Lindhorst, T. K.; Marradi, M.; Messner, P.; Molinaro, A.; Murphy, P. V.; Nativi, C.; Oscarson, S.; Penades, S.; Peri, F.; Pieters, R. J.; Renaudet, O.; Reymond, J.-L.; Richichi, B.; Rojo, J.; Sansone, F.; Schaffer, C.; Turnbull, W. B.; Velasco-Torrijos, T.; Vidal, S.; Vincent, S.; Wennekes, T.; Zuilhof, H.; Imberty, A., Multivalent Glycoconjugates as Anti-Pathogenic Agents. Chem. Soc. Rev. 2013, 42, 4709-4727.
12. Marradi, M.; Chiodo, F.; Garcia, I.; Penades, S., Glyconanoparticles as Multifunctional and Multimodal Carbohydrate Systems. Chem. Soc. Rev. 2013, 42, 4728-4745.
13. Lee, Y. C.; Lee, R. T., Carbohydrate-Protein Interactions: Basis of Glycobiology. Acc. Chem. Res. 1995, 28, 321-327.
14. Lis, H.; Sharon, N., Lectins: Carbohydrate-Specific Proteins That Mediate Cellular Recognition. Chem. Rev. 1998, 98, 637-674.
15. Cecioni, S.; Imberty, A.; Vidal, S., Glycomimetics Versus Multivalent Glycoconjugates for the Design of High Affinity Lectin Ligands. Chem. Rev. 2015, 115, 525-561.
16. El-Boubbou, K.; Zhu, D. C.; Vasileiou, C.; Borhan, B.; Prospero, D.; Li, W.; Huang, X., Magnetic Glyco-Nanoparticles: A Tool to Detect, Differentiate, and Unlock the Glyco-Codes of Cancer Via Magnetic Resonance Imaging. J. Am. Chem. Soc. 2010, 132, 4490-4499.
17. Gallo, J.; Garcia, I.; Padro, D.; Arnaiz, B.; Penades, S., Water-Soluble Magnetic Glyconanoparticles Based on Metal-Doped Ferrites Coated with Gold: Synthesis and Characterization. J. Mater. Chem. B 2010, 20, 10010-10020.
18. Dumur, F.; Guerlin, A.; Dumas, E.; Bertin, D.; Gigmes, D.; Mayer, C. R., Controlled Spontaneous Generation of Gold Nanoparticles Assisted by Dual Reducing and Capping Agents. Gold Bulletin 2011, 44, 119-137.

19. Duan, H.; Wang, D.; Li, Y., Green Chemistry for Nanoparticle Synthesis. *Chem. Soc. Rev.* 2015, 44, 5778-5792.
20. Manet, S.; Cuvier, A.-S.; Valotteau, C.; Fadda, G. C.; Perez, J.; Karakas, E.; Abel, S.; Baccile, N., Structure of Bolaamphiphile Sophorolipid Micelles Characterized with SAXS, SANS, and MD Simulations. *J. Phys. Chem. B* 2015, 119, 13113-13133.
21. Chen, J.; Song, X.; Zhang, H.; Qu, Y., Production, Structure Elucidation and Anticancer Properties of Sophorolipid from *Wickerhamiella Domercqiae*. *Enzyme Microb. Technol.* 2006, 39, 501-506.
22. Díaz De Rienzo, M. A.; Banat, I. M.; Dolman, B.; Winterburn, J.; Martin, P. J., Sophorolipid Biosurfactants: Possible Uses as Antibacterial and Antibiofilm Agent. *New Biotechnol.* 2015, 32, 720-726.
23. Kasture, M.; Singh, S.; Patel, P.; Joy, P. A.; Prabhune, A. A.; Ramana, C. V.; Prasad, B. L. V., Multiutility Sophorolipids as Nanoparticle Capping Agents: Synthesis of Stable and Water Dispersible Co Nanoparticles. *Langmuir* 2007, 23, 11409-11412.
24. Singh, S.; Patel, P.; Jaiswal, S.; Prabhune, A. A.; Ramana, C. V.; Prasad, B. L. V., A Direct Method for the Preparation of Glycolipid-Metal Nanoparticle Conjugates: Sophorolipids as Reducing and Capping Agents for the Synthesis of Water Re-Dispersible Silver Nanoparticles and Their Antibacterial Activity. *New J. Chem.* 2009, 33, 646-652.
25. Kumar, D. V. R.; Kasture, M.; Prabhune, A. A.; Ramana, C. V.; Prasad, B. L. V.; Kulkarni, A. A., Continuous Flow Synthesis of Functionalized Silver Nanoparticles Using Bifunctional Biosurfactants. *Green Chem.* 2010, 12, 609-615.
26. Baccile, N.; Noiville, R.; Stievano, L.; Bogaert, I. V., Sophorolipids-Functionalized Iron Oxide Nanoparticles. *Phys. Chem. Chem. Phys.* 2013, 15, 1606-1620.
27. Amstad, E.; Gehring, A. U.; Fischer, H.; Nagaiyanallur, V. V.; Hahner, G.; Textor, M.; Reimhult, E., Influence of Electronegative Substituents on the Binding Affinity of Catechol-Derived Anchors to Fe₃O₄ Nanoparticles. *J. Phys. Chem. C* 2011, 115, 683-691.
28. Amstad, E.; Gillich, T.; Bilecka, I.; Textor, M.; Reimhult, E., Ultrastable Iron Oxide Nanoparticle Colloidal Suspensions Using Dispersants with Catechol-Derived Anchor Groups. *Nano Letters* 2009, 9, 4042-4048.

- 1
2
3
4 29. Baccile, N.; Cuvier, A.-S.; Valotteau, C.; Van Bogaert, I. N. A., Practical Methods
5 to Reduce Impurities for Gram-Scale Amounts of Acidic Sophorolipid Biosurfactants.
6 Eur. J. Lipid Sci. Technol. 2013, 115, 1404-1412.
7
8
9 30. Dhasaiyan, P.; Le Griel, P.; Roelants, S.; Redant, E.; Van Bogaert, I. N. A.;
10 Prevost, S.; Prasad, B. L. V.; Baccile, N., Micelles Versus Ribbons: How Congeners
11 Drive the Self-Assembly of Acidic Sophorolipid Biosurfactants. Chem. Phys. Chem.
12 2017, 18, 643-652.
13
14
15 31. Napolitano, A.; D'Ischia, M.; Costantini, C.; Prota, G., A New Oxidation Pathway
16 of the Neurotoxin 6-Aminodopamine. Isolation and Characterization of a Dimer with a
17 Tetrahydro[3,4a]Iminoethanophenoxazine Ring System. Tetrahedron 1992, 48, 8515-
18 8522.
19
20
21
22 32. Bixner, O.; Lassenberger, A.; Baurecht, D.; Reimhult, E., Complete Exchange of
23 the Hydrophobic Dispersant Shell on Monodisperse Superparamagnetic Iron Oxide
24 Nanoparticles. Langmuir 2015, 31, 9198-9204.
25
26
27 33. El-Faham, A.; Funosas, R. S.; Prohens, R.; Albericio, F., Comu: A Safer and
28 More Effective Replacement for Benzotriazole-Based Uronium Coupling Reagents.
29 Chem. - Eur. J. 2009, 15, 9404-9416.
30
31
32 34. Kurzhals, S.; Zirbs, R.; Reimhult, E., Synthesis and Magneto-Thermal Actuation
33 of Iron Oxide Core-Pnipam Shell Nanoparticles. ACS App. Mater. Interfaces 2015, 7,
34 19342-19352.
35
36
37 35. Hyeon, T.; Lee, S. S.; Park, J.; Chung, Y.; Na, H. B., Synthesis of Highly
38 Crystalline and Monodisperse Maghemite Nanocrystallites without a Size-Selection
39 Process. J. Am. Chem. Soc. 2001, 123, 12798-12801.
40
41
42 36. Park, J.; An, K.; Hwang, Y.; Park, J.-G.; Noh, H.-J.; Kim, J.-Y.; Park, J.-H.;
43 Hwang, N.-M.; Hyeon, T., Ultra-Large-Scale Syntheses of Monodisperse Nanocrystals.
44 Nat. Mater. 2004, 3, 891-895.
45
46
47 37. Mondini, S.; Ferretti, A. M.; Puglisi, A.; Ponti, A., Pebbles and Pebblejuggler:
48 Software for Accurate, Unbiased, and Fast Measurement and Analysis of Nanoparticle
49 Morphology from Transmission Electron Microscopy (TEM) Micrographs. Nanoscale
50 2012, 4, 5356-5372.
51
52
53
54
55
56
57
58
59
60

- 1
2
3
4 38. Guinier, A.; Fournet, G., *Small-Angle Scattering of X-Rays*. John Wiley and Sons:
5 New York, 1955.
6
7 39. <http://www.sasview.org>.
8
9 40. Finger, L. W.; Hazen, R. M.; Hofmeister, A. M., *High-Pressure Crystal Chemistry*
10 *of Spinel (MgAl₂O₄) and Magnetite (Fe₃O₄): Comparisons with Silicate Spinel*s. *Phys.*
11 *Chem. Miner.* 1986, 13, 215-220.
12
13 41. Gulley-Stahl, H.; Hogan, P. A., 2nd; Schmidt, W. L.; Wall, S. J.; Buhrlage, A.;
14 Bullen, H. A., *Surface Complexation of Catechol to Metal Oxides: An ATR-FTIR,*
15 *Adsorption, and Dissolution Study*. *Environ. Sci. Technol.* 2010, 44, 4116-4121.
16
17 42. Valotteau, C.; Calers, C.; Casale, S.; Berton, J.; Stevens, C. V.; Babonneau, F.;
18 Pradier, C.-M.; Humblot, V.; Baccile, N., *Biocidal Properties of a Glycosylated Surface:*
19 *Sophorolipids on Au(111)*. *ACS Appl. Mater. Interfaces* 2015, 7, 18086-18095.
20
21 43. Slovetzkii, V. I., *Ir Spectra of Nitro Compounds*. *Bull. Acad. Sci. USSR, Div.*
22 *Chem. Sci.* 1970, 19, 2086-2091.
23
24 44. Shirmardi Shaghasemi, B.; Dehghani, E. S.; Benetti, E. M.; Reimhult, E., *Host-*
25 *Guest Driven Ligand Replacement on Monodisperse Inorganic Nanoparticles*.
26 *Nanoscale* 2017, 9, 8925-8929.
27
28 45. Santos-Carballal, D.; Roldan, A.; Grau-Crespo, R.; de Leeuw, N. H., *A Dft Study*
29 *of the Structures, Stabilities and Redox Behaviour of the Major Surfaces of Magnetite*
30 *Fe₃O₄*. *Phys. Chem. Chem. Phys.* 2014, 16, 21082-21097.
31
32 46. Valotteau, C.; Banat, I. M.; Mitchell, C. A.; Lydon, H.; Marchant, R.; Babonneau,
33 F.; Pradier, C.-M.; Baccile, N.; Humblot, V., *Antibacterial Properties of Sophorolipid-*
34 *Modified Gold Surfaces against Gram Positive and Gram Negative Pathogens*. *Colloids*
35 *Surf. B* 2017, 157, 325-334.
36
37 47. Chen, M.; Dong, C.; Penfold, J.; Thomas, R. K.; Smyth, T. J. P.; Perfumo, A.;
38 Marchant, R.; Banat, I. M.; Stevenson, P.; Parry, A.; Tucker, I.; Campbell, R. A.,
39 *Adsorption of Sophorolipid Biosurfactants on Their Own and Mixed with Sodium*
40 *Dodecyl Benzene Sulfonate, at the Air/Water Interface*. *Langmuir* 2011, 27, 8854-8866.
41
42 48. Baccile, N.; Selmane, M.; Le Griel, P.; Prevost, S.; Perez, J.; Stevens, C. V.;
43 Delbeke, E.; Zibek, S.; Guenther, M.; Soetaert, W.; Van Bogaert, I. N. A.; Roelants, S.,
44
45
46
47
48
49
50
51
52
53
54
55
56
57
58
59
60

1
2
3
4 Ph-Driven Self-Assembly of Acidic Microbial Glycolipids. *Langmuir* 2016, 32, 6343-
5 6359.

6
7 49. Abel, S.; Dupradeau, F.-Y.; Raman, E. P.; MacKerell, A. D.; Marchi, M.,
8
9 Molecular Simulations of Dodecyl-B-Maltoside Micelles in Water: Influence of the
10 Headgroup Conformation and Force Field Parameters. *J. Phys. Chem. B* 2011, 115,
11 487-499.

12
13
14 50. Bergin, R.; Carlstrom, D., Structure of the Pyrocatecholamines. li. Crystal
15 Structure of Dopamine Hydrochloride. *Acta Crystallogr., Sect. B* 1968, 24, 1506-1510.

16
17 51. Smith, M. B.; McGillivray, D. J.; Genzer, J.; Loesche, M.; Kilpatrick, P. K.,
18
19 Neutron Reflectometry of Supported Hybrid Bilayers with Inserted Peptide. *Soft Matter*
20 2010, 6, 862-865.

21
22
23 52. Reimhult, E.; Schroffenegger, M.; Lassenberger, A., Design Principles for
24 Thermo-responsive Core-Shell Nanoparticles – Controlling Thermal Transitions by Brush
25 Morphology. *Langmuir* 2019, 22, 7092-7104

26
27
28 53. Manet, S.; Cuvier, A.-S.; Valotteau, C.; Fadda, G. C.; Perez, J.; Karakas, E.;
29
30 Abel, S.; Baccile, N., Structure of Bolaamphiphile Sophorolipid Micelles Characterized
31 with SAXS, SANS, and MD Simulations. *J. Phys. Chem. B* 2015, 119, 13113-13133.

32
33 54. Penfold, J.; Chen, M.; Thomas, R. K.; Dong, C.; Smyth, T. J.; Perfumo, A.;
34
35 Marchant, R.; Banat, I. M.; Stevenson, P.; Parry, A.; Tucker, I.; Grillo, I., Solution Self-
36 Assembly of the Sophorolipid Biosurfactant and Its Mixture with Anionic Surfactant
37 Sodium Dodecyl Benzene Sulfonate. *Langmuir* 2011, 27, 8867-8877.

38
39
40 55. Amstad, E.; Gillich, T.; Bilecka, I.; Textor, M.; Reimhult, E., Ultrastable Iron Oxide
41 Nanoparticle Colloidal Suspensions Using Dispersants with Catechol-Derived Anchor
42 Groups. *Nano Letters* 2009, 9, 4042-4048.

43
44
45 56. Zirbs, R.; Lassenberger, A.; Vonderhaid, I.; Kurzhals, S.; Reimhult, E., Melt-
46 Grafting for the Synthesis of Core-Shell Nanoparticles with Ultra-High Dispersant
47 Density. *Nanoscale* 2015, 7, 11216-11225.

48
49
50 57. Ikeda, Y.; Sunakawa, T.; Tsuchiya, S.; Kondo, M.; Okamoto, K., Toxicological
51 Studies on Sophorolipid Derivatives. (I). Acute Toxicity, Eye Irritation, Primary Skin
52 Irritation, Skin Sensitization, Phototoxicity, Photosensitization, Mutagenicity of
53
54
55

1
2
3
4 Polyoxypropylene (12) [(2'-O-Beta-D-Glucopyranosyl-Beta-D-Glucopyranosyl)Oxy-]
5 Fatty Acid Ester-]. J. toxicol. Sci. 1986, 11, 197-211.

6
7 58. Gal, N.; Lassenberger, A.; Herrero-Nogareda, L.; Scheberl, A.; Charwat, V.;
8 Kasper, C.; Reimhult, E., Interaction of Size-Tailored PEGylated Iron Oxide
9 Nanoparticles with Lipid Membranes and Cells. ACS Biomat. Sci. Eng. 2017, 3, 249-
10 259.

11
12
13
14 59. Varela-Aramburu, S.; Wirth, R.; Lai, C. H.; Orts-Gil, G.; Seeberger, P. H.,
15 Straightforward and Robust Synthesis of Monodisperse Surface-Functionalized Gold
16 Nanoclusters. Beilstein J. Nanotech. 2016, 7, 1278-1283.

17
18
19 60. Reynolds, M.; Marradi, M.; Imberty, A.; Penades, S.; Perez, S., Influence of
20 Ligand Presentation Density on the Molecular Recognition of Mannose-Functionalised
21 Glyconanoparticles by Bacterial Lectin Bc2I-A. Glycoconj. J. 2013, 30, 747-757.

22
23
24 61. Ruiz, C. C., Sugar-Based Surfactants; Fundamentals and Applications. [In:
25 Surfactant Sci. Ser., 2009; 143]. CRC Press: 2008.

Graphical Abstract

